High-Temperature Modeling of Transport Properties in Hypersonic Flows

Daniel Dias Loureiro

Thesis to obtain the Master of Science Degree in

Aerospace Engineering

Supervisors: Prof. Mário António Prazeres Lino da Silva
Dr. Bruno Eduardo Lopez

Examination Committee

Chairperson: Prof. Fernando José Parracho Lau
Supervisor: Dr. Bruno Eduardo Lopez
Member of the Committee: Prof. Luís Paulo da Mota Capitão Lemos Alves

November 2015

Acknowledgments

I would like to acknowledge my advisors, Prof. Mário Lino da Silva and Dr. Bruno Lopez, whose support and guidance was fundamental for this work. Besides finding me financial support, it was Prof. Mário's hands-on attitude that motivated me forward when the situation looked the grimmest. But I especially owe the success of this work to Dr. Bruno Lopez and his infinite patience. More than a supervisor, Bruno was a true mentor, giving away his time to teach me everything from thermodynamics to advanced programming techniques, and for that, I feel privileged for having had the opportunity to work with him. I would also like to acknowledge Prof. Vasco Guerra for his input and long discussions on ambipolar diffusion. Finally, I would like to thank my lab mates Carlos Teixeira, João Vargas e Carolina Pinheiro for their contributions on my work, and also for their friendship and for making the long hours in the office more enjoyable.

I dedicate this thesis to my parents,
who never doubted me and supported all my academic adventures.

Resumo

Este trabalho estuda o escoamento hipersónico de plasmas em desequilíbrio que rodeia veículos espaciais em reentrada na atmosfera. O design deste género de veículos, dos escudos térmicos ou a previsão de efeitos de radio-blackout, dependem de modelos de transporte actuais, para a difusão de massa, viscosidade e condutividade térmica. Estes recursos foram implementados no código SPARK. Foram aplicados dois modelos aproximados para calcular coeficientes de transporte em gás fracamente ionizado: o modelo de Wilke/Blottner/Eucken, e o modelo de Gupta-Yos/Collision Cross-Section. Adicionalmente, foram revistos modelos para estimar os fluxos de difusão de massa, o que levou à proposta de um método com melhor consistência numérica, aplicado ao transporte de partículas carregadas. A implementação computacional fez uso do padrão *Estratégia* de programação orientada por objectos. A validação do método foi conseguida através da comparação directa dos coeficientes de transporte obtidos com modelos exactos. O código concebido foi aplicado com sucesso à simulação CFD do veículo RAM-C II, na qual ambos os modelos de transporte mostraram uma excelente correlação com os valores de densidade electrónica experimentais. Concluiu-se que ambos os modelos são igualmente apropriados para o caso de estudo, embora o modelo Gupta-Yos seja mais preciso quando os níveís de ionização são maiores, o que típicamente acontece para maiores velocidades de entrada.

Palavras-chave: Reentrada, CFD Hipersónico, Transporte, Diffusão Ambipolar , RAM-C II

Abstract

This work studies non-equilibrium hypersonic plasma flows surrounding space re-entry spacecrafts or planetary probes. The design of such vehicles, thermal protections or the estimation of radio blackout effects, relies on accurate hypersonic CFD codes with up to date transport models, for mass diffusion, viscosity and thermal conductivity. Such capabilities have been implemented in IPFN's hypersonic CFD code SPARK. Two approximate models have been implemented for the computation of the transport coefficients in a weakly ionized gas: the Wilke/Blottner/Eucken and the Gupta-Yos/Collision Cross-Section. Additional models to compute mass diffusion fluxes were reviewed, leading to the proposal of a method with improved numerical consistency, for charged particles transport. The implementation was done using an object-oriented *strategy* design pattern. It was successfully validated and assessed through direct comparison of the computed transport coefficients with exact models. The code was successfully applied to the CFD simulation of the RAM-C II re-entry vehicle, for which both transport models provided excellent correlation with experimental data for electronic density. Owing to the similar overall numerical efficiency of both models it was concluded that these are equally recommendable for this particular test case, although the Gupta-Yos will be more accurate for higher ionization levels, typically achieved for higher entry speeds.

Keywords: Re-entry, Hypersonic CFD, Transport, Ambipolar diffusion, RAM-C II

Contents

List of Figures

List of Tables

List of Symbols

Latin

C_P	Specific heat c. pressure, J·kg^{-1}·K^{-1}
C_V	Specific heat c. volume, J·kg^{-1}·K^{-1}
Δh°	Standard formation enthalpy, J·kg^{-1}
Kn	Knudsen number
Le	Lewis number
Ma	Mach number
$\mathrm{N}s$	Number of species
Re	Reynolds number
Sc	Schmidt number
$\vec{u}$	Mean flow velocity, m/s
$\vec{q_\mathrm{C}}$	Conduction heat flux, J·m^{-2}·s^{-1}
$\vec{q_\mathrm{D}}$	Diffusion heat flux, J·m^{-2}·s^{-1}
$\vec{J_s}$	Mass Diffusion Flux, kg·m^{-2}·s^{-1}
c_s	Mass fraction
D^a	Ambipolar Diffusion coefficient, m^2·s^{-1}
D_s	Diffusion coefficient, m^2·s^{-1}
E	Total energy, J·kg^{-1}
h	Enthalpy, J·kg^{-1}
M	Molar mass, kg/mol
m_s	Particle mass, kg
N	Number density, m^{-3}
n	Molar density, mol/m^3
P	Pressure, Pa
q_s	Charge per unit of mass, C/kg
R	Global gas constant, J·kg^{-1}·K^{-1}
r_s	Species gas constant, J·kg^{-1}·K^{-1}
T	Temperature, K
V_∞	Free stream velocity, m/s
x_s	Molar fraction

Greek

$\dot{\omega}_k$	Energy source term,J·s^{-1}·m^{-3}
$\dot{\omega}_s$	Mass source term,kg·m^{-3}·s^{-1}
ε	Internal/thermal energy, J·kg^{-1}
λ	Thermal Conductivity, J·s^{-1}·m^{-1}·K^{-1}
$[\tau]$	Viscous stress tensor, N·m^{-2}
μ	Viscosity coefficient, kg·m^{-1}·s^{-1}
ρ	Mass density, kg·m^{-3}
$\Delta_{sr}^{(1)}$	Diffusion collision term, m·s
$\Delta_{sr}^{(2)}$	Viscosity collision term, m·s
$\pi\overline{\Omega}_{sr}^{(1,1)}$	Diffusion collision cross-sections, Å^2
$\pi\overline{\Omega}_{sr}^{(2,2)}$	Viscosity collision cross-sections, Å^2

Subscripts

(none)	Global/total
s , r	Chemical species index
e	Free electrons
h	Heavy species
ion	Ionic species
m	Molecular species
k	Multi-temperature mode index
exc	Electronic excitation mode
rot	Rotational mode
tra	Translational mode
vib	Vibrational mode
∞	Free stream conditions

Vectorial Operators

$[\ ]$	Tensor
$\vec{\ }$	Vector
$^{\mathsf{T}}$	Transpose matrix
$\otimes$	Tensor Product
$[\mathrm{I}]$	Identity matrix
$\vec{\nabla}$	Gradient
$\vec{\nabla}\cdot$	Divergence

Physical Constants

k_{B}	Boltzmann const.: $1.380\,648\,8 \times 10^{-23}\ \mathrm{J \cdot mol^{-1}}$
e	Elementary Charge: $1.602\,176\,620\,8 \times 10^{-19}\ \mathrm{C}$
N_{A}	Avogadro const.: $6.022\,141\,29 \times 10^{23}\ \mathrm{mol^{-1}}$
R_{u}	Universal gas const.: $8.314\,462\,1\ \mathrm{J \cdot K^{-1} \cdot mol^{-1}}$

Non-SI Units

$\mathrm{Å}^2$	Square Angstrom $= 10^{-20}\ \mathrm{m^2}$
atm	Atmospheres $= 101\,325\ \mathrm{Pa}$
eV	Electron-Volt $= 1.602\,176\,565 \times 10^{-19}\ \mathrm{J}$
ft	Feet $= 0.3048\ \mathrm{m}$
in	Inch $= 0.0254\ \mathrm{m}$

Acronyms

SPARK	Software Package for Aerothermodynamics, Radiation and Kinetics
CCS	Collision Cross-Section
CFD	Computational Fluid Dynamics
DSMC	Direct Simulation Monte Carlo
OOP	Object-Oriented Programming
RAM-C II	Radio Attenuation Measurement
SCEBD	Self-Consistent Effective Binary Diffusion
TPS	Thermal Protection System

Chapter 1

Introduction

1.1 Atmospheric Entry Hypersonic Flows

An hypersonic flow is generally characterized by the presence of compressibility effects leading to the formation of strong and high temperature shock waves. This regime is commonly defined as having free stream speeds that exceeds a Mach number of 5.

Typical Earth re-entry velocities are in the range of 8 km/s (orbital speed) to 14 km/s (Mars return), corresponding to Mach numbers in the 20 to 50 range. The spacecraft entering planetary atmospheres are commonly designed with a forward facing blunt shape, which creates a detached bow shock in front of the body. This design allows to keep a stand-off distance between the shock and the vehicle surface, which alongside heat shielding materials allows it to survive the deceleration process. Figure 1.1 shows a schematic of the bow shock wave created on the re-entry of an Apollo-type capsule.

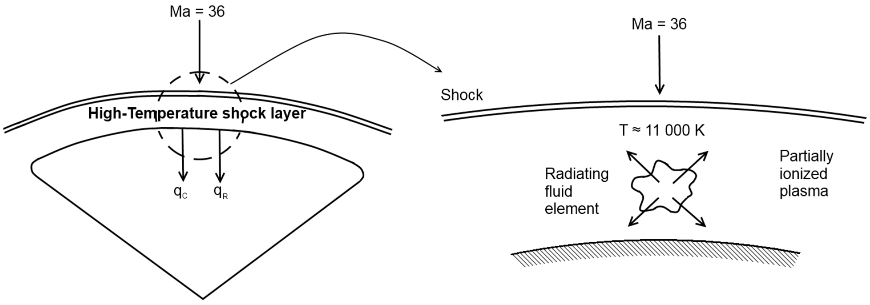

Figure 1.1: *Bow shock and high temperature shock layer. (adapted from ref. [1])*

In the shock layer the flow is quickly decelerated through the transfer of kinetic to thermal energy. Typical peak temperatures are in the 10^4 to 10^5 K order of magnitude. This energy transfer induces dissociation and partial ionization of molecules, leading to the formation of a plasma. In addition, the species internal degrees of freedom become excited, leading to the emission and/or absorption of radiation. This causes the flow properties to deviate from perfect gas values which is commonly referred as *high temperature effects*.

One of the main applications of hypersonic CFD simulations is the dimensioning of the thermal protection system (TPS) of the spacecraft. The two main mechanisms of heat transfer from the plasma to the aircraft are convection heating and radiation. In the scope of this work, only convection heating is considered, which is a direct result of the transport mechanisms being modeled. Radiation heating will become important for very energetic flows. The amount energy transfered through radiation can vary from 30% of the total heating calculated for the Apollo re-entry, to 95% for a probe entering the atmosphere of Jupiter [1]

Another effect that can be simulated using the present type of model is the electromagnetic blackout. While entering the atmosphere, ionization of the gas, will create a current of ions and electrons around the capsule, blocking the radio communications. Studies have been performed since the 1960's [2] on ways to alleviate this problem, commonly by forcing the recombination of the ions through the choice of materials for the TPS. To study electromagnetic blackout, an appropriate modeling of the diffusion of charged species is first required.

Laminar flow is commonly assumed, relying on a small Reynolds number in the stagnation region, and also on strong favorable pressure conditions, which delay the laminar-turbulent transition [3]. Due to the strong viscous effects, the thickness of the boundary layer is similar to the shock layer, causing a strong interaction between viscous and high temperature effects. Therefore the classical concept of boundary layer fails, and a fully viscous approach is necessary to model the hypersonic flow.

Due to the very small characteristic time scale involved, re-entry flows exhibit strong chemical and thermal non-equilibrium effects. Both are characterized by relaxation times, which are mainly dictated by the frequency of the interactions (collisions) between the particles. At the upper layers of the atmosphere, the gas is more rarefied and the collisions between particles are less frequent, meaning that stronger non-equilibrium effects will exist. At lower altitudes, although the gas is still reactive, non-equilibrium effects will dissipate more quickly.

During atmospheric entries, spacecrafts will cross a wide range of atmospheric density conditions. The region of interest for this work, is between 80 and 50 km in earth atmosphere, which is also the region where the deceleration becomes significant and the maximum convective heating will occur. At this altitude, the flow is continuous and can thus modeled by finite volume methods and the Navier-Stokes equations.

In the upper layers of the atmosphere, the flow transitions to the free molecular regime, meaning that the continuum assumption and the no-slip condition on the wall are no longer ensured. Therefore, the conventional CFD models are not applicable, and statistical models are used, such as Direct Simulations Monte Carlo method (DSMC) [4], carrying a greater computational cost.

An accurate CFD simulation of an atmospheric entry will have to consider all the phenomena described above, making it truly a multi-physics problem, requiring knowledge not only in fluid and thermo dynamics, but also chemistry, quantum mechanics, electromagnetism, radiation, statistical physics, etc. All these effects are coupled with strong interdependence, although it is not always practical to consider all the phenomena simultaneously due to prohibitive computational costs. Particularly, it is common to decouple the radiation effects in the Navier-Stokes model, as well as the electro-magnetic forces generated by the ionized flow. Other mechanisms such as electronic excitation or thermal non-equilibrium may in some cases be neglected, relying on previous knowledge for the particular flow regime being simulated.

1.2 Objectives and Road Map

This work aims to improve the capabilities of the SPARK code through the implementation of methods to compute transport properties of hypersonic flows.

The SPARK code — Software Package for Aerothermodynamics, Radiation and Kinetics — is maintained by the IPFN (Instituto de Plasmas e Fusão Nuclear) and is the only Hypersonic CFD code being developed in Portugal.

In a CFD simulation, the transport properties – viscosity, thermal conductivity and mass diffusion – can have a significant influence on the general behavior of the flow, and are fundamental for the estimation of important factors for spacecraft design and trajectory calculation, such as convective heating.

Exact physical models for computing these properties in high temperature and ionized gas exist, although approximate models are conventionally used for the sake of computational efficiency.

The models implemented in this work are the Wilke/Blottner/Eucken and Gupta-Yos/CCS, which are both valid for weakly ionized gases. Different methods to compute diffusion flux have also been assessed, considering the *ambipolar* diffusion effect for the charged species.

A thorough study was performed on the aforementioned physical models involved, and a review on the empirical data necessary as input for each of the transport models has been carried out.

The implementation was done using modern object-oriented programming techniques, focusing modularity and performance, while being verified and validated by direct comparison of with results from exact models and similar computations found on the literature.

Finally, the code is applied to the full CFD simulation of a typical test case – the RAM-C II experiment – allowing for the validation of the models against experimental data and other computational results obtained in previous works.

1.2.1 Review of Previous Work on the RAM-C II

Over the past two decades several studies have been performed on the simulation of the experimental data from the RAM-C II experiment, mainly focusing on the validation of thermal non-equilibrium and kinetic models. Particularly, Andrienko [3], Farbar et al. [5], and Soubrie [6], performed simulations with the same models used in this work, which have been considered for comparison purposes.

In the works of Walpot [7] and Farbar et al. [5], it is shown that catalicity effects — recombination of ions at the wall — have a great influence on the electron density flow, with improved results being obtained when full recombination is considered. Walpot [7] additionally shows that temperature prescribed at the wall does not have a significant impact on the results, within the $1000 - 1500\,\mathrm{K}$ temperature range. Josyula and Bailey [8], have shown that for the $61\,\mathrm{km}$ simulation with 7 species, the *ambipolar* effect on the diffusion of ions (eq. (2.38)) is not significant, predicting very similar results for both limiting cases.

A similar study has previously been done for the Stardust capsule, by Alkandry et al. [9], in which the Wilke/Blottner/Eucken and Gupta-Yos/CCS models are compared. They concluded that the two models were in good agreement for slow Earth entry speeds ($< 7\,\mathrm{km/s}$), and that the Wilke/Blottner/Eucken model would tend to over estimate the convective transfer at higher velocities. This study also recommends the use of the modified Fick law, similar to the one used in present work.

Chapter 2

Physical Models and Mathematical Formulation

A CFD simulation relies on well established theoretical models. For atmospheric re-entry flows, additional considerations need to be taken in order to fully capture all the aspects associated with the formation of a high temperature plasma, which are not considered in common finite volume methods.

Specifically, to capture the thermo-chemical processes and non-equilibrium effects, the gas is described by a multi-component and multi-temperature model, which introduces a greater complexity in the system of equations to be numerically solved. Although these models are out of the scope of this work, they are briefly introduced in section 2.1, since their basic understanding is fundamental throughout this work. This multi-component and multi-temperature description of the gas leads to a reformulation of all the basic thermodynamic relations which have been exhaustively defined in appendix A.1 for completeness. In this context, the system of partial differential equations used to model the flow is finally formulated in section 2.1.3, and also analyzed in more details in appendix A.3.

The transport phenomena, which is main focus of this work, are introduced in section 2.2. More specifically, the impact of transport processes on the governing equations is discussed and the underlying physical models for transport coefficients are presented. Two models are presented for the computation of the transport coefficients of weakly ionized high temperature gas, with different degrees of approximation: The Wilke/Blottner/Eucken model in section 2.2.1 and the Gupta-Yos/CCS in section 2.2.2.

Finally, in section 2.3, different models are reviewed to compute the mass diffusion fluxes while considering the effect of charged species. This analysis ultimately leads to the proposal of an improved method to compute these fluxes, in section 2.3.5.

2.1 Non-equilibrium Chemically Reacting Flow

2.1.1 Multi-Component Gas Mixture

In a chemically reacting flow, the gas is described by a multi-component model, i.e., a mixture of individual chemical species. This model assumes that the constituent species are mixed into a single phase allowing the gas properties (density, viscosity, etc.) to be represented by bulk properties, as function of the local chemical composition. General definitions and mathematical relations used to describe the gas composition and properties can be found on appendix A.1.

In this work an 11 species chemistry model is be used to model weakly ionized air, composed by the following chemical species:

$$N_2,\ O_2,\ N,\ O,\ NO,\ NO^+,\ N^+,\ O^+,\ N_2^+,\ O_2^+,\ e^-$$

Chemical Non-Equilibrium

Inside the shock layer, the time scales of the microscopic physical processes can be bigger than the characteristic macroscopic time of the flow. This may occur at the level of the chemical reactions, as the plasma forms due to the abrupt changes in temperature and pressure, meaning that even in steady state flow conditions, the chemical composition of a gas in a given region of the flow may have not reached chemical equilibrium. Consequently, the composition of the gas cannot be modeled simply as function of the gas state variables and chemical-kinetic models need to be applied. Using this type of model requires the solution of one mass conservation equation per chemical species considered (eq. (2.1)). The chemical-kinetic model then defines the rate of creation or consumption of each chemical species $\dot{\omega}_s$, based on the local state of the flow and characteristic time scales defined for each reaction.

2.1.2 Multi-Temperature Model

As the gas crosses the shock wave, a large part of the kinetic energy is transformed into thermal energy through excitation of the internal degrees of freedom. These internal degrees of freedom can be described as different reservoirs of thermal energy, which, depending on the particle type (mono-atomic, molecular or electron), are segregated into four main thermal energy modes — translational, rotational[1], vibrational and electronic excitation — which are represented in figure 2.1.

The mathematical formulation for the energy stored in each energy mode $\varepsilon_{k,s}$ as function of the corresponding temperature $T_{k,s}$ can be found in appendix A.1.3. Similar relations exist for definition of enthalpies $h_{k,s}$, specific heats $C_{\mathrm{P}k,s}$, $C_{\mathrm{V}k,s}$ and thermal conductivities $\lambda_{k,s}$, associated to each thermal energy mode k of the species s. Each model also establishes a correspondence between the different degrees of freedom of each species $\varepsilon_{k,s}(T_{k,s})$ and the global energy equation $\varepsilon_k(T_k)$ in which it participates. Examples of different models can be found in appendix A.2.

---

[1] The rotational, vibrational, and electronic excitation are commonly referred as internal modes, although the translational mode is also considered in the definition of the total internal energy, ε, (eq. (A.15))

(a) Translational Mode (b) Rotation Mode

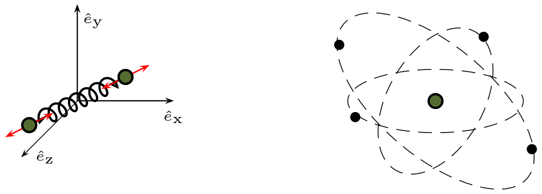

(c) Vibration Mode (d) Electronic Excitation Mode

Figure 2.1: *Graphical representation of the thermal energy modes. (From ref. [10])*

In the particular case of thermal equilibrium, all the thermal energy modes $\varepsilon_{k,s}$ are associated to the single temperature, $T_{k,s} = T$, and the energy in the flow is governed by a single equation (eq. (2.3)).

Thermal non-equilibrium

However, in a more general case, each chemical species in the gas may have each of its thermal energy modes excited differently, and the equilibrium is only reached after some energy exchanges, mainly through collisions. Energy exchanges between the different energy modes are characterized by relaxation times. Similarly to the chemical non-equilibrium, if the relaxation times are larger than the characteristic time of the flow, some regions of the domain may be in thermal non-equilibrium.

In the multi-temperature approach, the gas mixture is characterized by multiple temperatures T_k, each associated to a thermal non-equilibrium energy equation (eq. (2.4)). In each non-equilibrium mode the thermal energy ε_k is a function of the global temperature T_k. The source term $\dot{\Omega}_k$ defines the energy exchanges between the different modes. Additionally, coupling between the non-equilibrium modes and speciffic chemical reactions should also be considered.

Besides the added computational effort, the number of temperatures considered in non-equilibrium is mainly limited by the availability data used to describe the relaxation models. In this work, all the models are presented and implemented in a generic form, valid for any multi-temperature model.

2.1.3 Conservation Equations

The non-equilibrium chemically reacting flow is modeled by a system of partial differential equations, corresponding to the conservation of mass, momentum and energy. The complete system represents an extension of the classical Navier-Stokes equations, implying a continuum flow ($\mathrm{Kn} < 0.01$).

As described in the previous sections, one mass conservation equation is considered for each chemical species. An energy conservation equation is defined for the total energy, and for each of the non-equilibrium temperature energies, each one being associated to an non-equilibrium temperature. The momentum conservation is defined for the mean velocity of the flow $\vec{u}$ in vectorial form, resulting on one scalar equation for each of the spacial dimensions considered. A detailed analysis of these equations is done in appendix A.3.

- Mass of species s:

$$\frac{\partial}{\partial t}(\rho c_s) + \vec{\nabla} \cdot (\rho \vec{u} c_s) = \vec{\nabla} \cdot \vec{J_s} + \dot{\omega}_s \tag{2.1}$$

- Momentum :

$$\frac{\partial}{\partial t}(\rho \vec{u}) + \vec{\nabla} \cdot (\rho \vec{u} \otimes \vec{u}) = \vec{\nabla} \cdot [\tau] - \vec{\nabla} P \tag{2.2}$$

- Total energy :

$$\frac{\partial}{\partial t}(\rho E) + \vec{\nabla} \cdot (\rho \vec{u} E) = \vec{\nabla} \cdot \left(\sum_k \vec{q_{\mathrm{C}}}_k + \sum_s \vec{J_s} h_s + \vec{u} \cdot [\tau] - P\vec{u} \right) \tag{2.3}$$

- Non-equilibrium energy k:

$$\frac{\partial}{\partial t}(\rho \varepsilon_k) + \vec{\nabla} \cdot (\rho \vec{u} h_k) = \vec{\nabla} \cdot \left(\vec{q_{\mathrm{C}}}_k + \sum_s \vec{J_s} h_{s,k} \right) + \dot{\Omega}_k \tag{2.4}$$

2.2 Transport Properties

In the conservation equations defined in the previous section, the mass diffusion fluxes $\vec{J_s}$, the viscous stress tensor $[\tau]$ and the conduction heat fluxes $\vec{q_{\mathrm{C}}}_k$, are used to define the dissipative terms. Fundamentally, they model the natural transport of mass, momentum and energy by the random movement and collisions of the gas particles at microscopic level. The dissipative fluxes are generally defined as a function of the respective transport coefficients (table 2.1) and gradients:

- The mass diffusion flux $\vec{J_s}$ is modeled by Fick's Law of diffusion (reviewed in section 2.3):

$$\vec{J_s} = \rho D_s \vec{\nabla}(c_s) \tag{2.5}$$

- The viscous stress tensor $[\tau]$ assumes a Newtonian fluid and the Stokes hypothesis for the normal stresses:

$$[\tau] = \mu \left(\vec{\nabla} \vec{u} + (\vec{\nabla} \vec{u})^{\mathsf{T}} \right) - \frac{3}{2} \mu (\vec{\nabla} \cdot \vec{u}) \, [\mathrm{I}] \tag{2.6}$$

- The conduction heat flux in each non-equilibrium temperature mode $\vec{q_{\mathrm{C}}}_k$ is given by Fourier's Law of heat conduction:

$$\vec{q_{\mathrm{C}}}_k = \lambda_k \vec{\nabla} T_k \tag{2.7}$$

In the multi-temperature approach, a thermal conductivity λ_k is defined for each non-equilibrium temperature T_k, with the total thermal conductivity being given by summing up all the non-equilibrium and the equilibrium contributions.

Table 2.1: *List of dissipative fluxes and transport coefficients with dimensions in S.I. units*

		Dissipative Flux		Transport Coef.		Gradient	
Mass Diffusion	eq. (2.5)	$\vec{J}_s$	kg·m^{-2}·s^{-1}	D_s	m^2·s^{-1}	$\vec{\nabla}(c_s)$	m^{-1}
Viscosity	eq. (2.6)	$[\tau]$	N·m^{-2}	μ	kg·m^{-1}·s^{-1}	$\vec{\nabla} \cdot \vec{u}$	s^{-1}
Thermal Conductivity	eq. (2.7)	$\vec{q_{\mathrm{C}}}_k$	J·m^{-2}·s^{-1}	λ_k	J·s^{-1}·m^{-1}·K^{-1}	$\vec{\nabla}(T_k)$	K·m^{-1}

The transport coefficients therefore characterize the response of the gas to gradients in concentration, velocity and temperature. At high temperature, they are functions of the local chemical composition, temperature and pressure, requiring their computation in real-time during a CFD simulation.

The transport coefficients can accurately be determined using the classical Chapman-Enskog solution of the Boltzmann equation [11], which is valid for small Knudsen numbers. This model commonly requires the solution of a system of linear equations therefore being computationally expensive. The most effective approach is to use approximate mixture rules that allow to obtain the effective transport properties of gas mixture at specific composition, relying on simplifications to the Chapman-Enskog solution, valid for weakly ionized gases. Another approach is to use the iterative methods that are shown to be more accurate when the ionization is stronger [12].

In this work, the transport properties are computed using two different models based on mixing rules. The first approach is the Wilke/Blottner/Eucken model which is presented in section 2.2.1. The second is the Gupta-Yos/Collision Cross-Section model, in section 2.2.2.

Although the Gupta-Yos/CCS model is more detailed, the main advantage of the Wilke/Blottner/Eucken is its simplicity, since it requires a simpler implementation and a smaller amount of input data. While for the case of 11 species air all the necessary data is available for both models, this may not be the case for other chemistry models. The data sources used in this work are analized in section 3.2.

Independently of the model used to compute the transport coefficients, the definition of the mass diffusion flux requires special treatment to correctly model the diffusion of electrons in ionized gas, while ensuring numerical consistency of the model. These issues are addressed in section 2.3.

2.2.1 Wilke/Blottner/Eucken Model

This model was developed by C. Wilke [13] and consists on the application of kinetic theory to the first order Chapman-Enskog relation. The approximations are analogous to assuming that all interactions have the same (hard sphere) cross-section and ignoring inter-species interactions [14]. This approximations are expected to yield reasonable results for relatively small speeds with a maximum temperature of 10 000 K [15].

The global viscosity μ and the thermal conductivity λ_k for each global temperature is given by Wilke's semi-empirical mixing rule [13], which consists of a weighted sum on the individual species coefficients μ_s and $\lambda_{k,s}$:

$$\mu = \sum_s \frac{x_s \mu_s}{\phi_s} \qquad \text{and} \qquad \lambda_k = \sum_s \frac{x_s \lambda_{k,s}}{\phi_s} \tag{2.8}$$

where x_s is the species molar fraction and ϕ_s is calculated using the species molar masses M_s:

$$\phi_s = \sum_r x_r \left[1 + \left(\frac{\mu_s}{\mu_r}\right)^{1/2} \left(\frac{M_r}{M_s}\right)^{1/4}\right]^2 \left[8\left(1 + \frac{M_s}{M_r}\right)\right]^{-1/2} \tag{2.9}$$

The individual species viscosities are computed using Blottner's [16] model, in kg·m^{-1}·s^{-1}:

$$\mu_s(T) = 0.1 \exp\left((A_s \ln T + B_s)\ln T + C_s\right) \tag{2.10}$$

where T is the s-species translational temperature $T_{\mathrm{tra},s}$ and the values A_s, B_s and C_s are curve fitted coefficients, determined for each species. The sources for these coefficients are detailed in section 3.2.2.

The species' thermal conductivity for each degree of freedom $\lambda_{k,s}$ is determined using the generalized Eucken's relation [17], assuming a unit Schmidt number:

$$\begin{cases} \lambda_{\mathrm{tra},s} & = \frac{5}{2}\mu_s C_{\mathrm{V}\,\mathrm{tra},s} \\ \lambda_{\mathrm{rot},s=\mathrm{m}} & = \mu_s C_{\mathrm{V}\,\mathrm{rot},s} \\ \lambda_{\mathrm{vib},s=\mathrm{m}} & = \mu_s C_{\mathrm{V}\,\mathrm{vib},s} \\ \lambda_{\mathrm{exc},s\neq\mathrm{e}} & = \mu_s C_{\mathrm{V}\,\mathrm{exc},s} \end{cases} \tag{2.11}$$

where $C_{\mathrm{V}\,k,s}$ is the specific heat at constant volume of the s-species in each energy mode, given by equation (A.29). In thermal non-equilibrium, the different contributions of each species should be taken into the mixing rule (eq. (2.8)) according to the multi-temperature model used.

The mass diffusion coefficient for each species D_s is given by a single binary coefficient D, assuming a constant Lewis number, $\mathrm{Le} = 1.2$:

$$D_s = D = \frac{\mathrm{Le}\lambda}{\rho C_{\mathrm{P}}} \tag{2.12}$$

where ρ is the mixture's global density, C_{P} is the mixture total specific heat at constant pressure (eq. (A.26)), and λ is the total thermal conductivity. The Lewis number is a similarity parameter of the flow, corresponding to the ratio of the energy transport due to mass diffusion relative to thermal conduction.

2.2.2 Gupta-Yos/Collision Cross-Section Model

This model, as formulated by Gupta et al. [18], relies on a simplification of Chapman-Enskog solution, proposed by Yos [19], which employs an averaging of the interactions between particles of different species. Additional simplifications are made for computational optimization, which are known to be accurate only for non-ionized or weakly ionized flow. Although the latter simplifications can be avoided, the resulting cost of implementation would be comparable to the one of a exact solution of the Boltzmann equation [14], lessening its purpose. In these conditions, this model formulation is similar to the Wilke's mixing rule, but takes into consideration the true nature of the interactions between species of different kinds, by using the corresponding collision cross-sections.

For the computation of the transport coefficients, the strength of the interaction between each pair of species (s, r) is given by the collision terms $\Delta_{sr}^{(1)}$ and $\Delta_{sr}^{(2)}$ as function of the controlling temperature T_c:

$$\Delta_{sr}^{(1)} = \frac{8}{3}\left[\frac{2M_sM_r}{\pi R_\mathrm{u} T_c(M_s+M_r)}\right]^{1/2} \pi\overline{\Omega}_{sr}^{(1,1)}(T_c) \times 10^{20} \tag{2.13}$$

$$\Delta_{sr}^{(2)} = \frac{16}{5}\left[\frac{2M_sM_r}{\pi R_\mathrm{u} T_c(M_s+M_r)}\right]^{1/2} \pi\overline{\Omega}_{sr}^{(2,2)}(T_c) \times 10^{20} \tag{2.14}$$

where $\pi\overline{\Omega}_{sr}^{(1,1)}$ and $\pi\overline{\Omega}_{sr}^{(2,2)}$ are the average collision cross-sections in square angstroms ($\text{Å}^2 = 10^{-20}\,\text{m}^2$), which are calculated using Gupta's [18] curve fits. These quantities are detailed in section 3.2.1. The controlling temperature T_c in equations (2.13) and (2.14), is the heavy-species translational temperature $T_{\mathrm{tra,h}}$, except if the collision involves an electron, in which case the electron temperature $T_\mathrm{e} = T_{\mathrm{tra,e}}$ should be used. That is:

$$T_c = \begin{cases} T_{\mathrm{tra},s} & \text{if } s = \mathrm{h} \land r = \mathrm{h} \\ T_\mathrm{e} & \text{if } s = \mathrm{e} \lor r = \mathrm{e} \end{cases} \tag{2.15}$$

The gas mixture viscosity μ is then evaluated using the mixing rule:

$$\mu = \sum_s \frac{x_s m_s}{\sum\limits_r x_r \Delta_{sr}^{(2)}} \tag{2.16}$$

The translational mode of heavy species, λ_{tra}, and electrons, λ_e are given by:

$$\lambda_{\mathrm{tra}} = \frac{5}{2}\sum_{s\neq\mathrm{e}} \frac{x_s m_s C_{\mathrm{V\,tra},s}}{\sum\limits_r \alpha_{sr} x_r \Delta_{sr}^{(2)}} = \frac{15}{4} k_\mathrm{B} \sum_{s\neq\mathrm{e}} \frac{x_s}{\sum\limits_r \alpha_{sr} x_r \Delta_{sr}^{(2)}} \tag{2.17}$$

$$\lambda_\mathrm{e} = \frac{15}{4} k_\mathrm{B} \frac{x_\mathrm{e}}{\sum\limits_r \alpha_{er} x_r \Delta_{er}^{(2)}} \tag{2.18}$$

with:

$$\alpha_{sr} = 1 + \frac{[1 - M_s/M_r][0.45 - 2.54(M_s/M_r)]}{[1+(M_s/M_r)]^2} \tag{2.19}$$

The global thermal conductivities associated to the rotational, vibrational and electronic excitation modes of the heavy species, λ_{rot}, λ_{vib}, λ_{exc}, respectively, are evaluated by:

$$\lambda_{\text{rot}} = \sum_{s=\text{m}} \frac{x_s m_s C_{\text{V}\,\text{rot},s}}{\sum\limits_r x_r \Delta_{sr}^{(1)}} \tag{2.20}$$

$$\lambda_{\text{vib}} = \sum_{s=\text{m}} \frac{x_s m_s C_{\text{V}\,\text{vib},s}}{\sum\limits_r x_r \Delta_{sr}^{(1)}} \tag{2.21}$$

$$\lambda_{\text{exc}} = \sum_{s\neq\text{e}} \frac{x_s m_s C_{\text{V}\,\text{exc},s}}{\sum\limits_r x_r \Delta_{sr}^{(1)}} \tag{2.22}$$

In thermal equilibrium, the total thermal conductivity of the mixture λ is then given by:

$$\lambda = \lambda_{\text{tra}} + \lambda_{\text{e}} + \lambda_{\text{rot}} + \lambda_{\text{vib}} + \lambda_{\text{exc}} \tag{2.23}$$

If thermal non-equilibrium is considered, the thermal conductivity associated with each global temperature mode λ_k is calculated by taking the individual contributions of each species in equations (2.17) to (2.22) according to the multi-temperature model used.

The multicomponent mass diffusion coefficient D_{sr} is given, for each pair of species by:

$$D_{sr} = \frac{k_{\text{B}} T_c}{P \Delta_{sr}^{(1)}} \tag{2.24}$$

were P is the total pressure of the gas. This equation defines the diffusion velocity of each species relative to every other species. An averaged diffusion coefficient relative to the global remaining mixture D_s, can be obtained using:

$$D_s = \frac{1 - x_s}{\sum\limits_{r\neq s} \frac{x_r}{D_{sr}}} \tag{2.25}$$

The applicability of this equation is discussed in section 2.3, while purely numerical issues are addressed in section 3.4.

Although not explicitly required until now, the viscosity and thermal conductivity of a single species can also be calculated using this model, which can be seen as a particular case of the previous mixing rules for a gas mixture containing only one species. The viscosity for one species μ_s is given by:

$$\mu_s = \frac{5}{16} \frac{\sqrt{\pi m_s k_{\text{B}} T}}{\pi \overline{\Omega}_{ss}^{(2,2)}} 10^{20} \tag{2.26}$$

The translational thermal conductivity $\lambda_{\text{tra},s}$ is given by:

$$\lambda_{\text{tra},s} = \frac{5}{2} \mu_s C_{\text{V}\,\text{tra},s} = \frac{75}{64} k_{\text{B}} \frac{\sqrt{\pi k_{\text{B}} T / m_s}}{\pi \overline{\Omega}_{ss}^{(2,2)}} 10^{20} \tag{2.27}$$

and for the internal energy modes:

$$\lambda_{\text{rot},s=\text{m}} = \frac{8}{3} k_{\text{B}} C_{\text{V}\,\text{rot},s} \frac{\sqrt{\pi m_s k_{\text{B}} T}}{\pi \overline{\Omega}_{ss}^{(1,1)}} 10^{20} \tag{2.28}$$

$$\lambda_{\mathrm{vib},s=\mathrm{m}} = \frac{8}{3} k_{\mathrm{B}} C_{\mathrm{V\,vib},s} \frac{\sqrt{\pi m_s k_{\mathrm{B}} T}}{\pi \overline{\Omega}_{ss}^{(1,1)}} 10^{20} \tag{2.29}$$

$$\lambda_{\mathrm{exc},s\neq\mathrm{e}} = \frac{8}{3} k_{\mathrm{B}} C_{\mathrm{V\,exc},s} \frac{\sqrt{\pi m_s k_{\mathrm{B}} T}}{\pi \overline{\Omega}_{ss}^{(1,1)}} 10^{20} \tag{2.30}$$

The total thermal conductivity associated to a given species is then given by:

$$\lambda_s = \lambda_{\mathrm{tra},s} + \lambda_{\mathrm{rot},s} + \lambda_{\mathrm{vib},s} + \lambda_{\mathrm{exc},s} \tag{2.31}$$

2.3 Multi-Component Mass Diffusion

After implementing the models described in the previous sections, severe solver stability problems where found, particularly with the Gupta-Yos/CCS model when ionization was considered. The source of the instability was narrowed down to the mass diffusion flux of electrons.

By inspection of equations (2.14), (2.24) and (2.25), one can observe that the diffusion velocity is mainly dictated by the species mass and the averaged collision cross-section with other species. Since the mass of the electron is four to five orders of magnitude smaller than the heavy species', one can predict a diffusion velocity of the electron that is more than two orders of magnitude higher than the heavy species for a given collisional area. This high diffusion velocity then causes the accumulation of electrons in specific regions of the computational domain where their presence is not expected (e.g. upstream of the shock front), violating the quasi-neutrality assumption and possibly causing unrealistic chemical non-equilibrium situations.

This modeling of the electron diffusion has considered only the collision cross-section of the interactions with other species, neglecting the electrostatic forces that would be present in the described situation. It should be noted that this issue does not occur when the diffusion coefficients are calculated using the constant Lewis number model described in section 2.2.1 since this particular model inaccurately defines the same diffusion velocity for all species, independently of their mass and interactions with other species.

In this section the mass diffusion model are reformulated and different options found on the literature are analyzed, which stem from the investigation done while trying to solve the stability problems. Purely numerical issues related to the implementation of some of the models are also be addressed in section 3.4.

2.3.1 Stefan-Maxwell Model

An accurate modeling of the mass diffusion fluxes in a neutral multicomponent gas, is given by the solution of the Stefan-Maxwell equations, re-arranged to be solved for $\vec{J}_s$ and in terms of mass fraction gradient [20]:

$$\vec{J}_s = \rho D_s \vec{\nabla}(c_s) - \frac{c_s}{1-x_s} D_s \sum_{r \neq s} \left(\rho \frac{M}{M_r} \vec{\nabla}(c_r) + \frac{M}{M_r} \frac{\vec{J}_r}{D_{sr}} \right) \tag{2.32}$$

where D_{sr} are the binary diffusion coefficients, defined as function of the collision cross-sections (eq. (2.24)) and D_s is the effective mass diffusion coefficient of species s relative to the mixture, defined as:

$$D_s = \frac{1-x_s}{\sum\limits_{r \neq s} \frac{x_r}{D_{sr}}} \tag{2.33}$$

The solution of this system of equations can be computationally expensive and is therefore avoided, in favor of approximate methods.

2.3.2 Fick's Law

The most common approximate method is to use the classical Fick law of diffusion, using a mass diffusion coefficient D_s defined for each species:

$$\vec{J}_s = \rho D_s \vec{\nabla}(c_s) \tag{2.34}$$

This approach relies on the generalization of the Fick law – which was originally derived only for binary mixtures – and on the definition of the diffusion coefficient D_s which represents an averaged diffusion velocity of species s relative to the global diffusion velocity of the remaining species in the mixture. If the diffusion coefficient is determined assuming a constant Lewis number, as in the Wilke/Blottner/Eucken model (section 2.2.1), then the use of the generalized Fick model is straight forward. In the case of the more detailed model based on collisional interactions such as the Gupta-Yos/CCS model (section 2.2.2), the average diffusion D_s needs to be defined as function of the multicomponent diffusion coefficients D_{sr}. This definition is somewhat arbitrary, and different approaches can be found on the literature [21, 22, 23, 24], with different weighting methods.

The formulation used in this work (eq. (2.25)), which is the most commonly used [1, 20, 23, 9, 25], simply takes the effective diffusion definition from the exact Stefan-Maxwell equations (2.33). This approach corresponds the case when the second (dependent) term of the Stefan-Maxwell equations (eq. (2.32)) is neglected, reducing it to a trivial system. This model can also be derived with the assumption that all the other species move with the same velocity or are stationary [20].

2.3.3 Flux Normalization

Independently of the formulation used to define D_s, the generalized Fick model fails to ensure total mass conservation (eq. (A.35)), i.e.:

$$\sum_s \vec{J}_s = \vec{\varepsilon} \neq 0 \; ,$$

except for the very particular case in which all the species move with the same velocity, which conveniently occurs if a constant Lewis number model is used. Therefore, generally, the mass fluxes must be re-normalized, by distributing the flux residual $\vec{\varepsilon}$ on all the species fluxes, according to their mass fraction:

$$\vec{J}_s = \vec{J}_s^* - c_s \sum_r \vec{J}_r^* \tag{2.35}$$

where $\vec{J}_s^*$ is the *non-normalized* value of the species mass diffusion flux, given by Fick's Law (eq. (2.34)). By substituting equation (2.34), a *modified Fick model* is defined as:

$$\vec{J}_s = \rho D_s \vec{\nabla}(c_s) - c_s \sum_r \rho D_r \vec{\nabla}(c_r) \tag{2.36}$$

The works of Sutton et al. [20] and Alkandry et al. [9] show that this method is very accurate when compared with the exact Stefan-Maxwell solution for earth atmospheric entry cases.

2.3.4 Ambipolar Diffusion

In an ionized gas, the presence of charged species creates a local electric field in which other charged particles interact. This has the effect of enhancing the diffusion of the ions, which are *pulled* by the more mobile electrons, which in turn are slowed down by the heavier ions, and the two species diffuse with the same velocity, mainly dictated by the heavier species. This effect, known as *ambipolar* diffusion, consequently enforces a quasi-neutral diffusion flux, which can be formulated as:

$$\sum_s q_s \vec{J}_s = 0 \tag{2.37}$$

where q_s is the charge per unit of mass of species s. Since the electro-static forces are not considered in the conservation equations, this condition is only be respected if the *ambipolar* effect is artificially introduced in the calculation of the charged species diffusion. Assuming that the upstream flow is neutral and considering that the number of electrons and ions created due to chemical reactions is the same, the *ambipolar* effect also ensures the gas quasi-neutrality.

The classical derivation of a common *ambipolar* diffusion coefficient D^a can be found on F. Chen's work [26] for a binary mixture of ions and electrons. It is shown — by equating the fluxes of electrons and ions in terms of number density, while considering the induced electric field and neglecting the electron mass — that the *ambipolar* diffusion coefficient is given by:

$$D^a_{\mathrm{ion}} = \left(1 + \frac{T_{\mathrm{e}}}{T_{\mathrm{ion}}}\right) D_{\mathrm{ion}} \tag{2.38}$$

where D_{ion} is the ion *free* diffusion coefficient, based only on the collision cross-section, and T_{ion} and T_{e} are the translational temperatures of the ions and electron respectively. This equation is reduced to a simple factor of two if electronic thermal equilibrium is considered. In several works [15, 25, 22, 27], this model is generalized for multicomponent gas, and assuming $D^a_{\text{ion}} = 2D_{\text{ion}}$ even in thermal non-equilibrium conditions. Conversely, the derivation of the *ambipolar* diffusion coefficient shows that equation (2.38) is not valid if multiple ions are considered, unless it is assumed that all the ions have the same *free* diffusion coefficient and mobility, which generally is not true. Furthermore, G. Duffa [23] shows that the ratio between the diffusion coefficients is 2 only at relatively low temperatures ($<$ 5000 K) and tends to 1 at higher temperatures. In the work of Josyula and Bailey [8] it is also shown that for a 7 species mixture (where NO^+ is the only ionic species) the correction of the ion diffusion coefficient with equation (2.38) has no relevant effect on the electron density. This was found on the simulation of the RAM-C II probe, compared with the case in which the *free* diffusion coefficient of the ion is used.

When a single ionic species is considered, the diffusion coefficient for the electron reduces to $D^a_{\text{e}} = D^a_{\text{ion}}$. In the case of multiple ions, the diffusion velocity of the electron is then computed using [25, 22, 27]:

$$D^a_{\text{e}} = M_{\text{e}} \frac{\sum\limits_{s=\text{ion}} D^a_s x_s}{\sum\limits_{s=\text{ion}} M_s x_s} \tag{2.39}$$

This equation, which is obtained by equating the diffusion velocity of electrons with the mass-averaged diffusion velocity of ions [21], is convenient because it explicitly defines a value for the diffusion coefficient of the electron. Although, it is derived in the context of a diffusion flux formulation in terms of mole fraction x_s. For the present formulation of mass conservation in terms of mass fraction c_s, due to the dependency on the mass fraction gradient ∇c_s, equation (2.39) can only be obtained if the gradient of the global molar mass ∇M or density $\nabla \rho$ is neglected, while preassuming gas neutrality. Ultimately, this model does not accurately ensure the flux neutrality, especially considering that the ion diffusion fluxes would be “corrected” afterwards through equation (2.36). Actually, the resulting diffusion velocity of the electron has been found to be five orders of magnitude smaller than the heavy species, corresponding to the average mass ratio, which mitigates the solver stability problems, although this solution has not been adopted due to its inconsistency relative to the models used in this work.

An alternative was found in the works of Scalabrin [15] and Alkandry et al. [9], by avoiding the definition of a diffusion coefficient for the electron and using the flux neutrality condition (eq. (2.37)) to directly define the diffusion flux $\vec{J}_{\text{e}}$ as function of the total ionic flux:

$$\vec{J}_{\text{e}} = M_{\text{e}} \sum_{s=\text{ion}} \frac{\vec{J}_s}{M_s} \tag{2.40}$$

In the cited works, this equation is used after the *modified Fick model* (eq. (2.36)) to compute the ion fluxes, while neglecting the contribution of the electron flux on the normalization process. The final flux residual $\vec{\varepsilon}$ then would have a finite value, meaning that the mass conservation condition is no longer be respected. The residual value introduced by the electron diffusion to the total flux is assumed small due to the small mass of the electron. Although this approximation may be considered physically acceptable, it represents a mathematical inconsistency which is undesirable, as it may lead to solver instability. This inconsistency is obvious if a simple binary mixture of one ion and electrons is considered. In such case, equation (A.35), implied by the mass conservation equation and equation (2.40), necessary for flux neutrality, form the system of equations

$$\begin{cases} \vec{J}_{\mathrm{e}} = \vec{J}_{\mathrm{ion}} \\ \vec{J}_{\mathrm{e}} = \frac{M_{\mathrm{e}}}{M_{\mathrm{ion}}} \vec{J}_{\mathrm{ion}} \end{cases} \tag{2.41}$$

whose unique solution is $\vec{J}_{\mathrm{e}} = \vec{J}_{\mathrm{ion}} = 0$. This solution is physically valid in such gas mixture, considering that the diffusion velocity $D_s \vec{\nabla}(c_s)$ represents the velocity of the species relative to the mean flow velocity $\vec{u}$. Therefore, if the two species have the same diffusion coefficient and concentration, there is no deviation from $\vec{u}$. Yet, all the models presented return finite and different values for both diffusion fluxes in this case.

Another approximate model that considers the *ambipolar* effect is the the SCEBD method, proposed by Ramshaw [28]. This model directly defines the diffusion fluxes for all the species, completely replacing Fick's model. This option has not been explored since it would add much complexity on its implementation, having a dependency on the partial pressures and also because it cannot be employed with the Wilke/Blottner/Eucken model. Furthermore, the work of Alkandry [9] shows no evident improvement on the results relatively to the *modified Fick model*, on a comparison with the more rigorous Stefan-Maxwell model.

2.3.5 Improved Diffusion Model

Due to the mathematical inconsistency found in the diffusion models presented, an improved normalization method was derived, in order to use the generalized Fick's Law model for multicomponent diffusion while consistently ensuring both the mass conservation (eq. (A.35)) and flux neutrality (eq. (2.37)) imposed by the *ambipolar* effect .

Similarly to the *modified Fick model* presented previously, the *non-normalized* diffusion fluxes $\vec{J}_s^*$ are computed using the generalized Fick law (eq. (2.34)):

$$\vec{J}_s^* = \rho D_s \vec{\nabla}(c_s) \tag{2.42}$$

Then, the normalized diffusion fluxes $\vec{J}_s$ of the heavy species are computed by re-distributing the flux residual $\vec{\varepsilon}$ only on the heavy species fluxes, according to their mass fraction relative to total heavy species mass:

$$\vec{J}_{s \neq \mathrm{e}} = \vec{J}_s^* - \frac{c_s}{1 - c_{\mathrm{e}}} \vec{\varepsilon} \tag{2.43}$$

The electron diffusion flux is obtained using equation (2.40) with the normalized ion diffusion fluxes $\vec{J}_{\mathrm{ion}}$, thereby ensuring flux neutrality. Substituting equation (2.43) in (2.40), leads to:

$$\vec{J}_{\mathrm{e}} = M_{\mathrm{e}} \sum_{s=\mathrm{ion}} \frac{1}{M_s} \left(\vec{J}_s^* - \frac{c_s}{1-c_{\mathrm{e}}} \vec{\varepsilon} \right) \tag{2.44}$$

Finally, the flux residual $\vec{\varepsilon}$ is determined by imposing the mass conservation condition (eq. (A.35)) with the fluxes defined by equations (2.43) and (2.44):

$$\sum_s \vec{J}_s = \sum_{s\neq \mathrm{e}} \left(\vec{J}_s^* - \frac{c_s}{1-c_{\mathrm{e}}} \vec{\varepsilon} \right) + M_{\mathrm{e}} \sum_{s=\mathrm{ion}} \frac{1}{M_s} \left(\vec{J}_s^* - \frac{c_s}{1-c_{\mathrm{e}}} \vec{\varepsilon} \right) = 0 \tag{2.45}$$

which can be solved for $\vec{\varepsilon}$, giving:

$$\vec{\varepsilon} = \left(\sum_{s\neq \mathrm{e}} \vec{J}_s^* + \sum_{s=\mathrm{ion}} \frac{M_{\mathrm{e}}}{M_s} \vec{J}_s^* \right) \Bigg/ \left(1 + \sum_{s=\mathrm{ion}} \frac{M_{\mathrm{e}}}{M_s} \frac{c_s}{1-c_{\mathrm{e}}} \right) \tag{2.46}$$

In practice, the flux residual $\vec{\varepsilon}$ is computed first using equation (2.46) since it depends only on the *non-normalized* fluxes $\vec{J}_s^*$ given by equation (2.42), which is used to compute equation (2.43), and finally $\vec{J}_{\mathrm{e}}$ is computed using equation (2.40). With this solution, the normalization is done on the heavy species, while already “predicting” the diffusion flux of the electrons imposed by the *ambipolar* effect . Therefore both the flux neutrality and mass conservation conditions are simultaneously ensured.

It should be noted that the complexity introduced in the computation of the flux residual $\vec{\varepsilon}$, corresponds to simple summations that can be done simultaneously in a single cycle, with little computational cost. Furthermore, this method collapses into the *modified Fick model* (eq. (2.35)) for a non-ionized gas mixture. If all the heavy species have the same diffusion coefficient, as would occur if constant Lewis number model is used, the method simply enforces the flux neutrality condition. Finally, in the case of the binary single-ion/electron mixture, the flux values reduce to zero, as required by equations (2.41).

In this approach, the ion diffusion coefficients D_s used to define the *non-normalized* ion flux $\vec{J}_s^*$ may or may not include the *ambipolar* effect correction given by equation (2.38). In other words, the reciprocal effect of the presence of electrons on the ion diffusion velocity may optionally be neglected. This option was implemented, although it was not used in this work, according to the observations on the previous section.

Chapter 3

Implementation

The implementation of the models presented in chapter 2 in a functional and efficient computer program represents the largest part of the work load for this project. However, computer programming techniques are often not covered in this kind of report due to its detachment from the actual aerospace physics. Although specific details related to the actual programing language used are not covered, this chapter aims to cover the aspects related to the implementation of the transport models, and present some of the lessons learned from long debugging hours, before its actual application.

Section 3.1 contains a general overview the structure and programing philosophy of the implementation done.

The models transport models implemented require large amount of input data for which different sources can used. Section 3.2 reviews the data used in this work is reviewed and assesses its quality.

Section 3.3 presents some numerical test performed for code verification. These allowed for the detection of programming bugs and also arithmetic artifacts that led to numerical stability problems. The proposed solutions for these problems are presented in section 3.4.

3.1 Structure and Programming Techniques

The models presented in chapter 2 were implemented in the SPARK code — Software Package for Aerothermodynamics, Radiation and Kinetics — currently maintained at IPFN.

The SPARK code integrates several physical models required for the simulation of high speed non-equilibrium flows. Due to the highly multi-physics nature of such flows, the design and implementation of SPARK is focused on both modularity and performance. Therefore, the code has been written in Fortran 2003 language making use of modern oriented-object programming techniques. The code is structured as a collection of independent modules, each one devoted to a specific physical model or numerical method yet sharing a common data structure which facilitates both inter-module communication and easy integration of new functionalities.

Following the object oriented philosophy of SPARK, the procedures used to compute the transport properties are encapsulated in a self-contained module, i. e., the `transport` object, which is by itself also designed with extension in mind, to allow for an easy integration of future transport models.

In the `transport` object, some public methods are defined, wich are the procedures or functions that are available to the "user" of the program. The user of the `transport` object, in the context of a full hypersonic flow simulation, is SPARK's `gas` object, which is responsible for the computation of all the gas properties. Alternatively, the user can also be any other application code, for example the one used to generate some of the results and evaluate computational effort for the present report.

The public methods available to the user are:

- `Construct` Allocates and defines the necessary variables in memory according to the user input, setting-up the `transport` object for later use, such as Lewis number or the option indicator to consider *ambipolar* diffusion.
- `Set_Model` Sets the transport model to be used, Wilke/Blottner/Eucken, Gupta-Yos/CCS, etc.
- `Compute_Transport` Computes all the transport properties simultaneously, μ, λ_k and D_s.
- `Compute_Viscosity` Computes the viscosity coefficient μ
- `Compute_ThermalCond` Computes the the thermal conductivity coefficients λ_k
- `Compute_MassDiffusion` Computes the diffusion coefficients D_s

The different procedures for computing individual properties are available for convenience, although only the general `Compute_Transport` is optimized for performance, since a lot of intermediate results on the calculations are shared between the coefficients (e. g. the collision terms, equation (2.13)). Therefore only this procedure is used in a full-scale simulation.

Independently of the transport model being used, the `Compute_Transport` always has the following general inputs and outputs:

- Inputs: `mixture`, ρ, c_s, T_k, P_k, $C_{\mathrm{P}k}$
- Outputs: μ, λ_k and D_{sr}

where `mixture` is another SPARK object, containing all the empirical or pre-processed thermodynamic data related to the chemical species contained in the gas.

The variables with the k and s subscript are vectors and matrices with size depending on the multi-temperature model used and the number of chemical species in the mixture. All the necessary information, such as the correspondence of the index in these vectors to specific species or temperature modes, is retrieved from the `mixture` object. This allows an implementation that is generic and flexible enough to be used with any multi-component and multi-temperature model.

The description of the `transport` object is until now independent of the actual model being used, i. e., it only defines an interface for a generic transport model. The actual implementation implementation of the transport models, which for the present work are the Wilke/Blottner/Eucken and the Gupta-Yos/CCS, is done in independent sub-modules, using a Strategy Pattern [29].

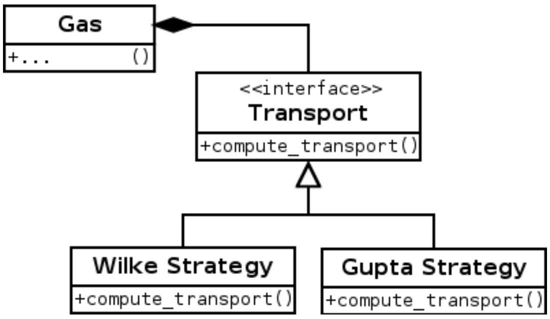

Figure 3.1: *Transport object implementation in a Strategy Pattern*

In each transport strategy object, the actual implementation of the transport models is done using normal procedural programing techniques.

For both models the `mixture` object also contains the input data required, which is the Blottner coefficients for the Wilke/Blottner/Eucken model and the collision cross-section curve fits for the Gupta-Yos/CCS model. This data is read from a data base and stored in memory when the `mixture` is constructed, being efficiently accessed and used every time the `compute_transport` procedure is called.

3.2 Review of Input Data

3.2.1 Gupta's Collision Cross-Section Curve fits

For each collision pair, two collision cross-sections are calculated: $\pi\overline{\Omega}^{(1,1)}_{sr}(T)$, refered as "Diffusion collision cross-sections", is used to model the diffusion coefficients and the thermal conductivity of the internal thermal energy modes (rotational, vibrational and electronic excitation); $\pi\overline{\Omega}^{(2,2)}_{sr}(T)$ is refered as "Viscosity collision cross-sections", and is used to model the viscosity and the translational thermal conductivity.

The collision cross-sections used in this work have been curve fitted by Gupta et al. [18]. This set of coefficients is widely used, although studies have shown that they are becoming obsolete and better data sets have recently been developed [30]. Gupta's fits are given by the following expressions in square angstroms (Å^2):

$$\pi\overline{\Omega}^{(1,1)}_{sr}(T) = \exp D_{\overline{\Omega}^{(1,1)}_{sr}} T^{\left[A_{\overline{\Omega}^{(1,1)}_{sr}} (\ln T)^2 + B_{\overline{\Omega}^{(1,1)}_{sr}} \ln T + C_{\overline{\Omega}^{(1,1)}_{sr}}\right]} \tag{3.1}$$

$$\pi\overline{\Omega}^{(2,2)}_{sr}(T) = \exp D_{\overline{\Omega}^{(2,2)}_{sr}} T^{\left[A_{\overline{\Omega}^{(2,2)}_{sr}} (\ln T)^2 + B_{\overline{\Omega}^{(2,2)}_{sr}} \ln T + C_{\overline{\Omega}^{(2,2)}_{sr}}\right]} \tag{3.2}$$

For collisions between charged species (ions and/or electrons) the cross-sections are modeled according to a Coulomb potential, meaning that the collision cross-section is mainly dictated by attractive or repulsive electrostatic interactions. If a high concentration of free electrons is present, the strength of the interaction is reduced by the shielding effect, as a function of the electronic pressure. These curve fits are provided for a limiting electron pressure $P_\mathrm{e} = P_\mathrm{em}$ given by:

$$P_\mathrm{em} = 0.0975 \left(\frac{T_\mathrm{e}}{10^3} \right)^4 \qquad [\mathrm{atm}] \tag{3.3}$$

which corresponds to maximum electronic pressure for which the model is valid, although most aerospace applications should fall below this limit. For electron pressures lower than P_em, the curve fits for the pair of charged species needs to be corrected by the shielding factor $\ln \Lambda$:

$$\overline{\Omega}_{sr}^{(l,l)}(P_\mathrm{e}) = \overline{\Omega}_{sr}^{(l,l)}(P_\mathrm{em}) \times \ln \Lambda(P_\mathrm{e}) \tag{3.4}$$

given by:

$$\ln \Lambda(P_\mathrm{e}) = \frac{1}{2} \ln \left[2.09 \times 10^{-2} \left(\frac{T_\mathrm{e}}{10^3 P_\mathrm{e}^{1/4}} \right)^4 + 1.52 \left(\frac{T_\mathrm{e}}{10^3 P_\mathrm{e}^{1/4}} \right)^{8/3} \right] \tag{3.5}$$

where P_e is in atm units and can be calculated using equation (A.11) with the appropriate unit conversion. This correction results in larger cross-sections for the charged species, since a lower electron pressure means that the shielding effect is weaker and the charged particles interact at larger distances. The numerical implementation of this correction factor may lead to arithmetic issues, which are addressed in section 3.4.

All the curves have been fitted for the 1000 K to 30 000 K temperature range. To avid incorrect extrapolation of the curves beyond their validity range, the collision cross-sections computed at $T < 1000$ K are set to a constant value corresponding to $T = 1000$ K. The same method is applied for $T > 30\,000$ K, although this limit is not expected to be reached in the current application. The absence of this limitation on the lower temperature side has led to solver stability issues, particularly for electron-neutral interactions. Although some of the fits may actually be valid beyond this range, the same limit has been applied for all the pairs, for consistency.

The different curve fits have been plotted as function of temperature in figures B.1(a) to B.2(c) in appendix B.1. For the interactions between neutral species (figs. B.1(a) and B.1(b)), precise curve fits are given for every pair, which tend to cluster according to the atomicity of the involved species. The only exceptions are the diffusion components ($\pi\overline{\Omega}_{sr}^{(1,1)}$) of the pairs O–O and N–N, for which the curve fits ave been set equal to O^+–O and N^+–N respectively, to account for electronic excitation effects [18].

The interactions between neutral and ionic species (fig. B.2(a)) are generally given by a single pair of viscosity and diffusion curve fits, with the exceptions of O^+–O and N^+–N, and also the diffusion cross-sections of NO^+–NO, for which particular curve fits are given.

For the interactions between charged species (fig. B.2(b)), the collision cross-section should be determined according to the charge of the species involved, resulting in three different curves for each collision cross-sections type [30]. Although, for the diffusion curve-fits, the same coefficients are given for the three types of interaction, while for the viscosity curves a different set of coefficients is given for the collisions involving the electron. This data suggests that the values are approximately the same for any of the cases. Nonetheless it should be noticed that these collision cross-sections can be several orders of magnitude higher than the ones involving neutral species. In this figure, the shielding effect correction has also been applied for air in chemical equilibrium at 1 atm (fig. 4.1), showing a one order of magnitude difference relative to the uncorrected values.

For the collisions between electrons and neutral species B.2(c), both the viscosity and collision cross-sections are given by the same coefficient set. The curve fits for O_2, O and NO are given in piecewise functions; a large discontinuity was found between the two branches, especially for the NO case. Therefore, to avoid possible numerical stability issues, the discontinuities were eliminated by adjusting the $D_{\overline{\Omega}_{sr}^{(1,1)}}$ and $D_{\overline{\Omega}_{sr}^{(2,2)}}$ coefficients on the higher temperature branch. This solution is not necessarily the most accurate, although a very small influence on the results is expected.

3.2.2 Blottner Viscosity Curve Fits

The Blottner model for viscosity was originally proposed [16] for a 6 species model for air, (N_2, O_2, N, O, NO, NO^+), and therefore does not specify the viscosity coefficients for the remaining ionic species and electron. A more comprehensive data set can be found on the work of Gupta et al. [18], where the viscosity coefficients have been calculated using the collision cross-sections described before and equation (2.26), and then fitted to a curve with the formulation given by Blottner (eq. (2.10)):

$$\mu_s(T) = 0.1 \exp\left((A_s \ln T + B_s) \ln T + C_s\right) \tag{2.10}$$

Consequently, the equivalent shielding correction needs to be applied for the viscosity of the ionic and electron species:

$$\mu_s(P_\mathrm{e}) = \mu_s(P_\mathrm{em}) \times \frac{1}{\ln \Lambda(P_\mathrm{e})} \tag{3.6}$$

where $\ln \Lambda(P_\mathrm{e})$ is given by equation (3.5).

The curve fits using this set of coefficients have been plotted as function of temperature in figures B.3 and B.4 in appendix B.2. Considering the shielding correction, the viscosity of the ionic species at higher temperatures is about 10 times smaller than the neutrals, although they can be several orders o magnitude smaller at lower temperatures, as a result of the electrostatic forces, as evidenced by the corresponding collision cross-sections.

A comparison has been made between the viscosity coefficients obtained using the original Blottner curve fits [16] and the Gupta et al. data [18], used in this work . The relative error is shown in percentage of the Gupta values, in figure 3.2. These results show a good agreement between the two data sets for the neutral species, with errors within 1% for the temperature range of interest. For NO^+, in which the shielding effect correction has been considered for air at 1 atm, the difference is much more significant at lower temperatures, due to the exponential behavior of the curve given by the collision cross-section model, although the results still tend to agree around 16 000 K .

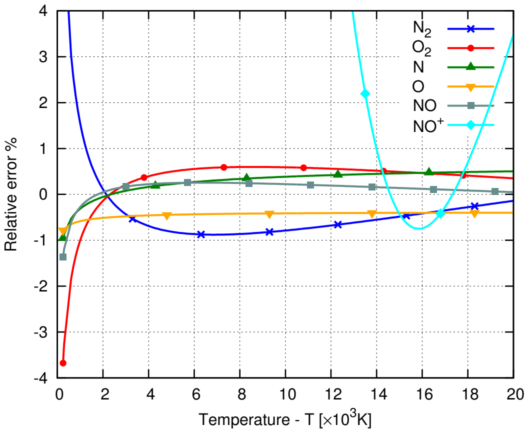

Figure 3.2: *Relative error between Blottner species viscosity curve fits [16] and the values based on collision cross-sections [18]*

3.2.3 Eucken relation

Although the generalized Eucken relation has been used with the Wilke mixing rule (eq. (2.11)), the thermal conductivity of the individual species λ_s can also be computed from the collision cross-sections, using equation (2.31).

A comparison was made between the total conductivity λ_s given by the two models for all the chemical species, considering that the influence of the viscosity coefficient can be eliminated, since both models use the same data source to compute it. The effect of the shielding correction for the charged species can also be ignored since the same correction factor would be applied in both cases. The translational component of the thermal conductivity is mathematically the same by inspection of equation (2.27), therefore having no effect on the conductivity of free electrons. For all the heavy species the conductivity for internal degrees of freedom in the Gupta-Yos model are computed considering the true nature of the interactions between particles through the use of the collision cross-section $\pi\overline{\Omega}_{sr}^{(1,1)}$.

The results, in figure B.5 of appendix B.3, show that the generalized Eucken relation overestimates the conductivity of the atomic species, while underestimating for the molecular and ionic species. Yet, at lower temperatures, both models generally agree, corresponding to the temperature range in which only the translational and rotational modes are excited. Consequently, the global thermal conductivities obtained using the Eucken relation are less reliable at higher temperatures, but the accuracy depends on the chemical composition of the mixture, since there seems to be a compensation effect between the atomic and the ionic/molecular species.

In this model a unitary reciprocal Schmidt number has been considered, as it is most commonly done for this model [15, 9]. However, a value $\mathrm{Sc}^{-1} = 1.32$ has been recomended by Svehla [31, 17]. In line with the previous observations, this correction would mainly improve the results for the molecular and ionic species.

Finally, in fig. B.5(d), it can be observed that the thermal conductivity of free electrons is significantly higher than the remaining species, although it is greatly reduced by the shielding effect correction, which would nonetheless affect the ionic species equally.

3.3 Code Verification Tests

An application code was developed which directly uses the transport object, as described in section 3.1. It is capable of performing independent computations for a given gas composition, and providing numerical comparisons of results, for a consistent and systematic code and model verification.

The results generated by this tests are the used for the model validation and comparative analysis performed in section 4.1.

Independent computations where made for each transport model assuming thermal equilibrium and a multi-temperature model. For the multi-temperature model five temperatures where considered, corresponding to the four thermal energy modes of heavy species and also the translational mode of free electrons, although all the temperatures were set to the same numeric value, artificially imposing a thermal equilibrium $T_{\mathrm{tra}} = T_{\mathrm{rot}} = T_{\mathrm{vib}} = T_{\mathrm{exc}} = T_e = T$. This approach also allows the retrieval of the individual contributions of the thermal conductivities associated with each temperature mode. The two cases returned the same numerical value for all the transport properties, as expected.

Similarly the code was tested for a scalar computation in each individual temperature of the range and compared to a one-dimensional computation of the complete temperature range, simulating a 1D computation. For this test the results were also exactly the same, as expected.

It was also verified that the procedure for computing all the transport properties return the same result as the procedures for computing each transport coefficient independently.

In all the computations at 300K, the molar fraction of all species except O_2 and N_2 was set to exactly zero, and also to the smallest representable number for the numerical precision used, to trigger possible arithmetic errors, such as the ones presented in section 3.4.

3.4 Numerical Issues on the Transport Model

In the implementation of the transport models exposed in section 2.2, some of the equations required special attention due to mathematical singularities, for which the computer returns *NaN* (Not-a-Number) or infinity (arithmetic Overflow), such as in a division by zero, causing the simulations to immediately "crash". This kind of problem most often appeared when the equations involve the composition of the gas, requiring that the composition variable to have a finite value. In practice, the whole computational domain outside the shock region has zero or near-zero particle number for most of the species that result from the chemical reactions.

One common workaround to this kind of problem is to define an arbitrary minimum residual value to all the molar fractions, e.g. [24]:

$$x_s = x'_s + \delta \qquad \text{with:} \qquad \delta = 1 \times 10^{-12} \tag{3.7}$$

Yet, this solution was avoided due to the loss of precision and unpredictability of the actual effects on a full simulation, specially considering that the code is intended to have the flexibility to work in a wide range of situations and not only the earth entry with a 11 species air model used in this work. Instead, all the sources of mathematical singularities were analyzed considering the chain of intermediate results, localizing them in just a few operations, which were reformulated as follows, in order to avoid this problem.

Shielding effect correction

As presented in section 3.2.1, equation (3.5), defines the correction factor $\ln\Lambda$ as a function of the electronic partial pressure P_e and temperature T_e:

$$\ln\Lambda(P_\varepsilon) = \frac{1}{2}\ln\left[2.09\times10^{-2}\left(\frac{T_\mathrm{e}}{10^3 P_\mathrm{e}^{1/4}}\right)^4 + 1.52\left(\frac{T_\mathrm{e}}{10^3 P_\mathrm{e}^{1/4}}\right)^{8/3}\right] \tag{3.5}$$

which is used to correct the collision cross-sections $\overline{\Omega}_{sr}^{(l,l)}$ for interactions between charged species (eq. (3.4)), and also the viscosity coefficient μ_s of charged species with $1/\ln\Lambda$ (eq. (3.6)).

This function has a singularity $\ln\Lambda = \infty$ when $P_\mathrm{e} = 0$. The physical meaning of the singularity is that in the absence of free electrons there is no shielding effect and, according to the Coulomb Law, the two particles interact at infinite distances resulting in a infinite collision cross-section. Yet, from the computational point of view this is not acceptable, since if the mass fractions of the charged species have a residual value, the shielding correction must be applied with a finite value even if the corresponding electronic pressure is numerically zero, possibly due to numerical truncation error. Additionally, even if one ensures that the computation is done only if $P_\mathrm{e} \neq 0$, it was observed that the intermediate result

$$\Phi = \left(\frac{T_\mathrm{e}}{10^3 (P_\mathrm{e})^{1/4}}\right)^4 \tag{3.8}$$

can easily cause an arithmetic overflow when the value of P_e is very small, specially considering that the electronic pressure is computed in Pa units and locally converted to `atm`. Therefore Φ needs to be limited to a "computationally safe" value while being high enough to be physically valid. The solution was to reformulate equation (3.5) as:

$$\ln\Lambda(P_\mathrm{e}) = \frac{1}{2}\ln\left[2.09\times10^{-2}\,\Phi + 1.52\,\Phi^{2/3}\right] \tag{3.9}$$

with Φ defined as:

$$\Phi = \begin{cases} P_0 \times 10^{-12}\dfrac{T_\mathrm{e}^4}{P_\mathrm{e}} & \text{if } \Phi \leq \Phi_\mathrm{max} \\ \Phi_\mathrm{max} & \text{if } \Phi > \Phi_\mathrm{max} \end{cases} \tag{3.10}$$

where P_e is in Pa, with $P_0 = 1.013\,250\times10^5$ Pa as conversion factor to `atm`. Φ_max is the largest value numerically representable with the current precision. In Fortran it is given by the intrinsic function `huge`, which in double precision returns a value of $1.797\,69\times10^{308}$. With this intermediate limitation, the maximum value of the shielding correction for the same precision is $(\ln\Lambda)_\mathrm{max} = 3.529\,57\times10^2$. This limit is low enough to avoid any numerical representation problems in the subsequent calculations, while being high enough to be physically accurate, specially considering that such values can only occur in computational points where the presence of the charged species is very low, therefore having very little significance in the global transport properties of the gas.

Effective Mass Diffusion coefficient

As described in sections 2.2.2 and 2.3, equation (2.25) is used to compute a averaged mass diffusion coefficient of each species relative to the remaining mixture:

$$D_s = \frac{1 - x_s}{\sum\limits_{r \neq s} \frac{x_r}{D_{sr}}} \tag{2.25}$$

In this equation there are two division operations which can potentially lead to numerical problems.

The first, is in the individual contributions to the summation on the main denominator x_r/D_{sr}. By inspection of equation (2.24), one can predict a very small value of D_{sr} if both the collision term $\Delta_{sr}^{(1)}$ and total pressure P have very high values, which may lead to $D_{sr} = 0$ due to numerical truncation error. If simultaneously the value of x_r is also zero, the result is a mathematical indetermination $0/0$, numerically returning a NaN. Although this is very unlikely, due to the order of magnitude of the involved physical quantities, this situation was prevented by considering the current species r contribution to the summation only if $D_{sr} > 0$.

The second error occurs when only one species is present, with $x_s = 1$ and $x_{r \neq s} = 0$, resulting again in a 0/0 indetermination, now on the main fraction. This is particularly evident in a chemistry model in which the gas is made of only one species in the upwind conditions, such as in a N_2–N mixture. Additionally, the trivial relation obtained from the molar fraction definition

$$1 - x_s = \sum_{r \neq s} x_r \tag{3.11}$$

is not always met, due to numerical truncation errors on the computation of the molar fractions x_s from the main composition variable c_s (eq. (A.5)) when the values of c_s approach zero. With double precision errors were found in the 10^{-170} order of magnitude. Although this error is not physically significant, this inconsistency on the numerator and denominator causes random results on the computation of D_s in such gas composition conditions, leading to solver instability.

To solve this problem the equation was re-formulated to the analytically equivalent:

$$D_s = \frac{\sum\limits_{r \neq s} x_r}{\sum\limits_{r \neq s} \frac{x_r}{D_{sr}}} \tag{3.12}$$

which ensures that any numerical truncation error is equally present on both the numerator and denominator. Still, in the case of $\sum\limits_{r \neq s} x_r = 0$, the equation is still undefined and results in a $0/0$ indetermination. In that case the diffusion coefficient is set to zero. This represents a discontinuity on the function, that would be evident on a cell interface where this summation goes from zero to a finite value. Yet, it is expected to have little influence on the solution, specifically on the mass diffusion fluxes, assuming that the mass fraction gradient is small in that situation. Tests done with different gas models, including N_2–N case show no stability problems related to this issue. An alternative solution would be to use the equation (3.7) workaround, although that would simply define a equally heightened mean value which would still represent a discontinuity.

Electron ambipolar diffusion

Although it was not used in the final implementation of the transport model, the equation used to compute the diffusion coefficient of the electron assuming the *ambipolar* effect (section 2.3) also presents numerical issues.

$$D_{\mathrm{e}}^{a} = M_{\mathrm{e}} \frac{\sum\limits_{s=\mathrm{ion}} D_s^a x_s}{\sum\limits_{s=\mathrm{ion}} M_s x_s} \tag{2.39}$$

Again, there is a $0/0$ indetermination when the summation of all the ions molar fraction is zero. In this case the diffusion coefficient of the electron is set to zero, similarly, and with the same limitations, as in equation (3.12). Although, from a physical perspective, if a residual number of electrons is present in the absence of ions, their diffusion velocity should be the one based only on collision cross-section, i.e., the *free* diffusion coefficient D_{e}. But if this solution is considered, it causes solver instability due to the very high diffusion velocity of the free electron, which was the original motivation to consider the *ambipolar* effect.

Chapter 4

Results

This chapter presents the results obtained with the models implemented. In section 4.1, a verification and validation analysis is made on the transport coefficients obtained by direct application of the implemented routines, for air at atmospheric pressure, in chemical equilibrium, as function of temperature. The transport models were then applied to the full simulation of the RAM-C II test case, using the CFD capabilities of the SPARK code. The experiment details, simulation parameters and the analysis of results are presented in section 4.2. Section 4.3 presents a comparison of the computational efficiency between the two transport models.

4.1 Model Verification and Validation

To verify and validate the implementation, the transport coefficients were evaluated using the two models described in section 2.2. An 11 species air gas mixture was used at the standard atmospheric pressure 101 kPa, and in the temperature range of 300 K to 20×10^3 K. The mixture equilibrium composition was obtained using the NASA CEA code [32] and is plotted in fig. 4.1.

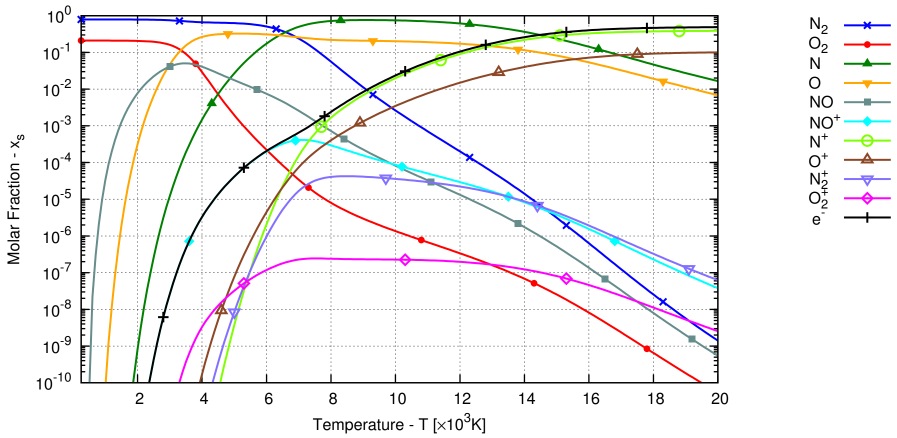

Figure 4.1: *Equilibrium composition of 11 species air, 1 atm*

Recent works by Palmer and Wright provide the results used for comparison for the global viscosity

[14] and total thermal conductivity [17]. Besides using the same mixing rules used in the present work, calculations using a multicomponent Chapman-Enskog method are also provided, which is used as an *exact solution* reference. Assuming a similar equilibrium composition as function of temperature, the only significant difference between the present and the reference work is the collision cross-section data.

For the diffusion coefficients, no relevant reference data has been found for the same conditions, therefore the results are simply qualitatively compared between the different models.

4.1.1 Viscosity

The comparison of the present results for global viscosity with the references for the same mixing rules show a general agreement in behavior, although a small deviation is generally observed. Since a similar offset behavior is observed for both models, the deviation can be attributed to variations in collision cross-section data.

The Chapman-Enskog solution also depends on the collision cross-section data, therefore, this deviation should be considered as part of the error of the present results relative to the that solution.

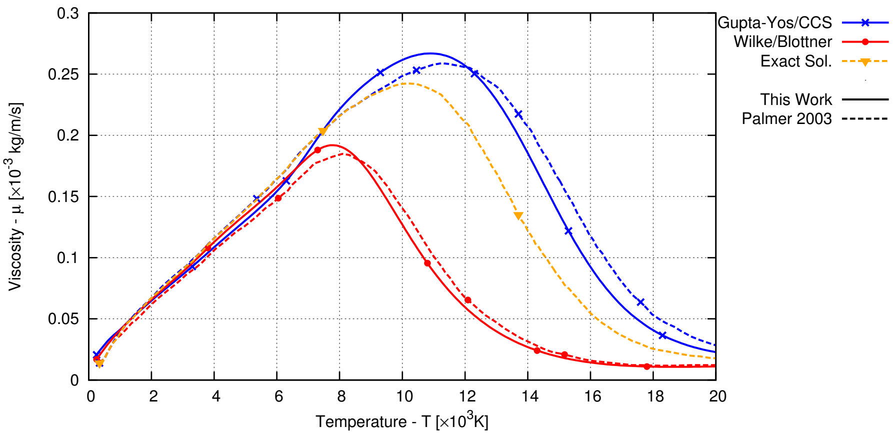

Figure 4.2: *Comparison of models for global viscosity μ, equilibrium air 1 atm.*

More severe discrepancies start to occur when the ionization becomes significant, around 8000 K corresponding to an electron mole fraction $x_{\mathrm{e}} = 10^{-3}$. The Gupta-Yos/CCS model holds a prediction within 10% of the exact value until the peak viscosity value is reached at 10 000 K. Beyond this point the difference can be as high as 50% at 14 000 K. Generally, this model over-estimates the exact solution. The Wilke/Blottner/Eucken model shows a much stronger sensitivity to ionization, with a difference larger than 10% at 8000 K, while at 12 000 K the viscosity is under-predicted with a 75% difference. Bellow 6000 K ($x_{\mathrm{e}} =< 10^{-4}$), both models are within 5% of the exact value.

4.1.2 Thermal Conductivity

Figure 4.3 shows the contribution of the different thermal energy modes to the total thermal conductivity. At low temperature, while the translational mode of heavy species has the same behavior for both models, the small differences in the total conductivity are due to the rotational and vibrational modes which are lower in the Wilke/Blottner/Eucken model. Above 6000 K, the electronic excitation mode has an important contribution, although the contribution predicted by the Wilke/Blottner/Eucken model is affected by the over-estimation of this mode for the atomic species and under-estimation for the ionic species, as observed in section 3.2.3. Above 16 000 K the thermal conductivity is manly dictated by the free electrons, although their contribution to the global conductivity is evaluated differently by the two mixing rules.

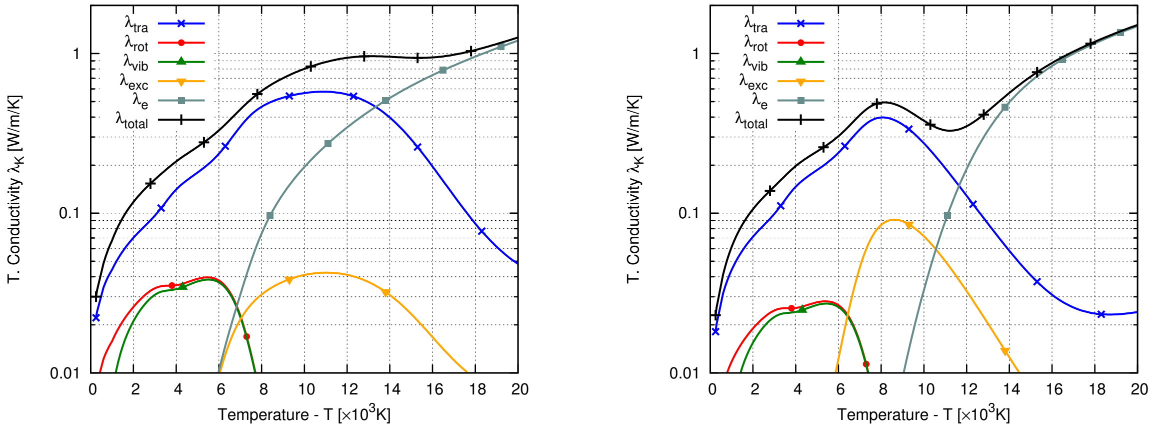

(a) Gupta-Yos/CCS

(b) Wilke/Blottner/Eucken

Figure 4.3: *Contributions to the global thermal conductivity of the internal degrees of freedom λ_k, equilibrium air 1 atm.*

The total thermal conductivities assuming thermal equilibrium are plotted in fig. 4.4 and again compared with the reference calculations [17] using the same models and and also the exact Chapman-Enskog solution.

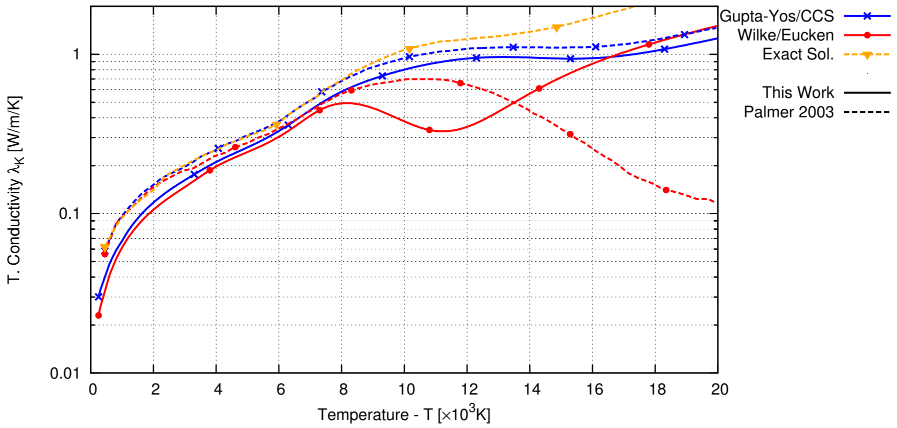

Figure 4.4: *Comparison of models for total thermal conductivity λ, equilibrium air 1 atm.*

Again, a generalized offset of the results can be observed for the mixture rules, specially for the Gupta-Yos mixing rule, which shows a nearly constant difference along the whole temperature range, and also for the Wilke/Blottner/Eucken model before ionization. Again, this deviation is attributed to differences in the collision cross-section data. De facto, at low temperatures, a better agreement of the results is observed when compared with multicomponent solutions found in other works [33, 18, 12, 23].

The large disagreement in the behavior of the solution using the Wilke/Blottner/Eucken model at high temperatures can also be explained by differences in the collision cross-section data. At these temperatures, the thermal conductivity is mainly dictated by the free electrons contribution, which for this mixing rule is particularly sensitive to the electron-electron interaction, as a consequence of the mixing rule not considering inter-species interactions. This is not the case with the Gupta-Yos/CCS model, where possible large differences in the electron-electron collision cross-section are concealed by the contribution of electron-heavy interactions.

Within the uncertainty introduced by the use of different collision cross-section data sets, it can be observed that both models are accurate at lower temperatures, and start to deviate from the exact solution when ionization begins, at $8000\,\mathrm{K}$. Although, similarly to the viscosity results, the Gupta-Yos/CCS model delivers reasonably good predictions to higher temperatures than the Wilke/Blottner/Eucken model.

4.1.3 Mass Diffusion

As described in section 2.3, due to the *ambipolar* effect, the heavy species and the electrons are treated differently. The diffusion coefficients are presented for the heavy species, while not considering the *ambipolar* effect on the ions (eq. (2.38)) which in this case would have been a simple factor two correction. A more detailed analysis is done subsequently for the electron diffusion.

Heavy Species

The mass diffusion of heavy species evaluated with both models are plotted in fig. 4.5. With the Gupta-Yos/CCS model the diffusion coefficient is defined independently for each chemical species. The results show that the diffusion coefficient of ionic species is substantially smaller than for neutral species, which is a direct consequence of the much larger collision cross-sections caused by the electrostatic interactions.

For the Wilke/Blottner/Eucken model, the diffusion coefficient is set equally for all species according to the constant Lewis number model. This model delivers reasonable results when compared with the Gupta model for neutral species, although a higher discrepancy is observed for ions, which have lower diffusion velocities. For high temperatures the model generally over-predicts the diffusion coefficient, although none of the models is expected to be valid for such ionization levels.

Electrons

As described in section 2.3, the diffusion coefficient of the free electrons is not directly defined by the transport models. Instead, it is calculated by enforcing a neutral flux as a consequence of the *ambipolar*

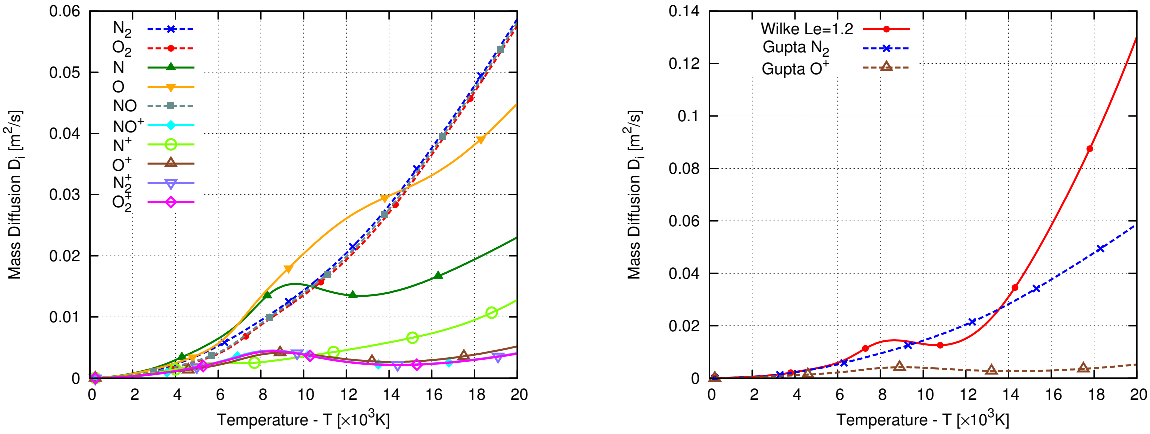

(a) Gupta-Yos/CCS

(b) Wilke/Blottner/Eucken

Figure 4.5: *Diffusion coefficients D_s of the heavy species, equilibrium air 1 atm.*

effect. Nonetheless, an equivalent diffusion coefficient can be calculated if the gradient of the electron mass fraction c_e is known:

$$D_e^{eq} = \frac{\vec{J}_e}{\rho \vec{\nabla} c_e} \tag{4.1}$$

The mass fraction gradient has been obtained from the gas composition along the stagnation line in the simulation of the RAM-C II test case (section 4.2). The same gas composition data has been used to compute the diffusion coefficients that would be obtained when no *ambipolar* effect is considered – the *free* difusion coefficient given by equation (2.25) or equation (2.12) – and also the electron *ambipolar* coefficient explicitly given by equation (2.39).

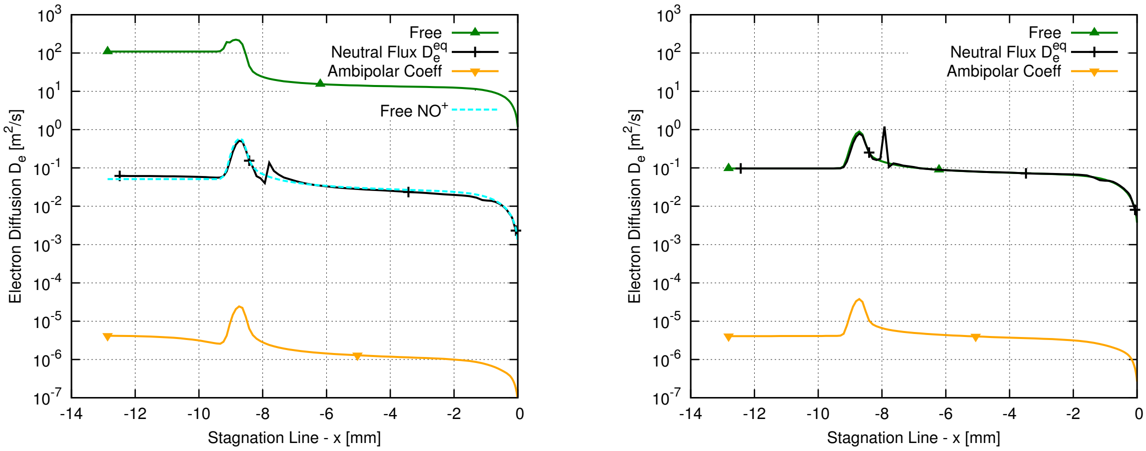

(a) Gupta-Yos/CCS

(b) Wilke/Blottner/Eucken

Figure 4.6: *Model comparison for electron diffusion coefficient D_s , RAM-C II stagnation line.*

Firstly, figure 4.6(a) clearly shows how the reduced mass of the electron results in a diffusion coefficient 2 to 3 orders of magnitude higher than NO^+ if no *ambipolar* diffusion effects are considered. For the Wilke/Blottner/Eucken model (fig. 4.6(b)), this is does not occur since the same diffusion coefficient is considered for every species, including the electrons.

When equation (2.39) is applied, the resulting electron diffusion coefficient is 4 orders of magnitude smaller than the heavy species, clearly showing the inadequacy of this model, at least for the diffusion flux formulation used in this work, although it may still be valid if the mass conservation equation is defined in terms of mole fraction [21].

For the Gupta-Yos/CCS model, the equivalent diffusion coefficient D_{e}^{eq}, obtained by ensuring flux neutrality, effectively sets the diffusion velocity of the electron to values with order of magnitude similar to the *free* ions. Although, it introduces a change in the curve behavior for both transport models. While the general behavior of all the curves is dictated by the variation of the diffusion coefficient as function of temperature — showing a maximum value around $-9\,\mathrm{mm}$ that corresponds to the shock wave — the sharp oscillation introduced at $-8\,\mathrm{mm}$ is a consequence of intense gradients of the combined ion concentration that result from the chemical reactions and ionization processes occurring immediately after the shock. This means that the diffusion velocity of the electrons is effectively adjusted to follow the ionic fluxes, as intended.

Generally, but especially for the Gupta model, these results justify the analysis done in section 2.3 and validate the use of the flux neutrality method.

4.2 Aplication Case: RAM-C II experiment

The RAM-C (Radio Attenuation Measurement) experiments where a series of tests conducted in the late 1960's by the Langley Research Center (LARC) [2, 34]. The goal of the experiments was to to study the blackout effect by measurements of electron density in the plasma around blunt body spacecrafts. Three flight experiments where conducted, using similar sphere-cone probes with a radius of $0.15\,\mathrm{m}$, a cone angle of $9\,°$ and $1.3\,\mathrm{m}$ of length, at re-entry speeds around $7.6\,\mathrm{km/s}$. The second experiment, RAM-C II, is of particular interest because a Beryllium heat sinking cap was used to cover the nose of the aircraft, avoiding the pollution of the flow with ablation products from the heat-shield.

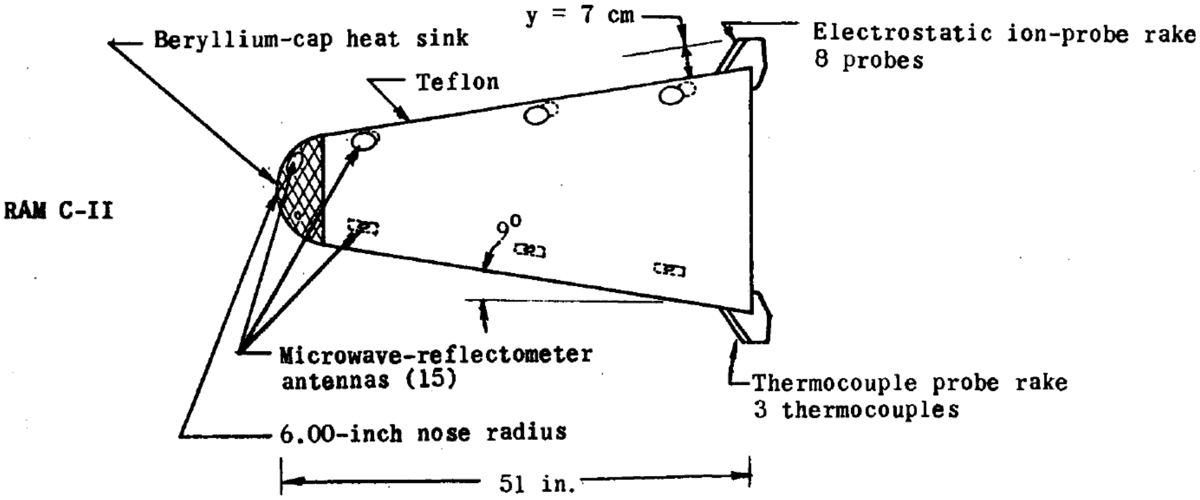

Figure 4.7: *Schematic of RAM-C II payload configuration (from ref. [2])*

In this experiment the electron density was measured using two sets of sensors. The first are microwave reflectometer antennas, used to measure the maximum electron density in four different locations along the body of the aircraft. The second is a rake of eight electrostatic Langmuir probes located near the rear, which measure the electron density at different distances from the wall. A large uncertainty is associated to the measurements made with the electrostatic probes (represented by error bars), due to oscillations caused by the rotation of the aircraft with a non-zero angle of attack.

A large amount of data was collected from these experiments in a wide range of flight conditions, which has been serving as a classical benchmark for hypersonic CFD codes over the past decades. Therefore several studies are available on simulations of this experiment, providing additional data to be used for validation and model comparison. The trajectory points most commonly simulated are at the altitudes of 81, 71 and $61\,\mathrm{km}$, corresponding to Mach numbers of 28.3, 25.9 and 23.9, respectively. While the flow velocity is approximately constant ($7.6\,\mathrm{km/h}$), the free-stream pressure varies greatly between these trajectory points, with Knudsen numbers ranging from 3×10^{-2} to 1.5×10^{-3}.

Consequently, for the higher altitudes the flow has stronger rarefaction and non-equilibrium effects, requiring more complex models which are out of the scope of this work. To minimize these factors, the $61\,\mathrm{km}$ flight condition has been chosen for the validation and comparison of the transport models in the present work, although chemical and thermal non-equilibrium are still expected to be significant. This altitude also corresponds to the trajectory point where the maximum temperatures and stronger ionization levels are reached, and for that reason is the most relevant for the comparison of the transport models. Unfortunately, for the same reason, this is also the trajectory point where the least experimental data is available, due to the saturation of some sensors, specially in the electrostatic rake.

4.2.1 Simulation Parameters and Models

All the simulations are performed for the 61 km flight condition, using the parameters in table 4.1.

Table 4.1: *Simulation parameters*

h, km	Ma	Kn	V_∞, m/s	T_∞, K	P_∞, Pa	ρ_∞, kg/m^3	$x_{\mathrm{N_2}}$	$x_{\mathrm{O_2}}$	T_{wall}, K
61	24	4×10^{-4}	7650	244	19.3	2.73×10^{-4}	0.79	0.21	1200

The following models are used to describe the transport phenomena in thermal equilibrium simulations:

– Wilke/Blottner/Eucken, assuming $\mathrm{Le} = 1.2$, defined in section 2.2.1

– Gupta-Yos/CCS, defined in section 2.2.2

– inviscid (Euler equations)

An additional thermal non-equilibrium simulation is performed using the Gupta-Yos/CCS model, with the Park two temperature model (T_{TR}, T_{EV}) [35]. The thermal relaxation models used are:

– Vibration-Chemistry: Candler 1989 [36]

– Vibration-Translation: Lee 1985 [37] and Millikan-White 1963 [38]

– Electron-Translation: Appleton 1968 [39]

The Park 2001 [40] kinetic model is used for all the simulations.

As described in section 3.2, the data from Gupta 1990 [18] is used for both the collision cross-sections and the Blottner viscosity coefficients.

The mass diffusion fluxes are calculated using the *modified Fick Law* along with the proposed improved normalization method, as described in section 2.3.5. The *ambipolar* effect on the diffusion of ions (eq. (2.38)) was generally not applied, although the effect on electrons is always considered, by ensuring flux neutrality (eq. (2.44)). Nonetheless the *ambipolar* effect on ions has been considered, only where indicated, for the verification of its effect.

An isothermal boundary condition is considered, with a prescribed wall temperature of 1200 K [5]. A non-catalytic boundary condition at the wall is generally applied. Where explicitly indicated, the effect of a super-catalytic condition is verified for some of the results, in order to show the limiting cases for the catalytic effect. The super-catalytic condition is introduced by imposing at the wall the chemical composition of the free stream.

4.2.2 Mesh and Convergence Study

All the simulations have been performed using an implicit numerical scheme. The time step of each iteration is determined by the CFL number as function of the smallest cell size. For all the simulations a small CFL number was required for the initial iterations, typically 1, which is later raised up to 100.

The convergence of the solution is evaluated by the root-mean-square value of the residual of the system of equations. For the mesh convergence study, the solutions have a maximum 10^{-4} residual. For all other test cases the solution residuals are between 10^{-7} and 10^{-10}, except for the inviscid simulation for which a residual of 10^{-5} was the lowest achievable .

All the simulations performed use similar structured cartesian meshes composed of a single block. Since the position of the shock does not significantly change with the different models for the same flight conditions, the meshes generated for different simulations are very similar. One of them is represented in figure 4.8.

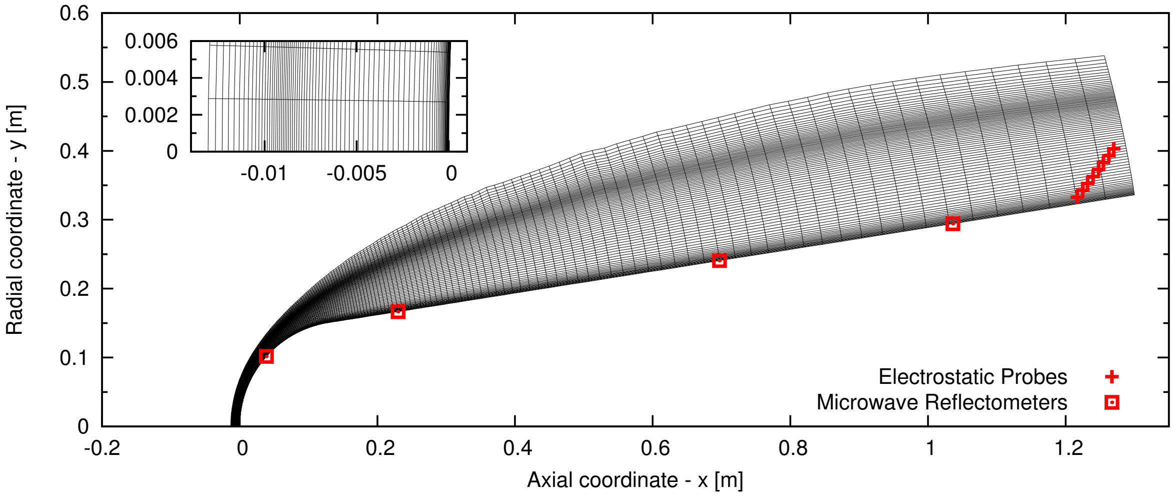

Figure 4.8: *Computational mesh, with* 80×160 *cells and adapted at shock wave and boundary layer. Detail on stagnation line. Location of the experimental probes.*

The corresponding location of the experimental probes is also plotted in fig. 4.8 for reference. The simulated microwave reflectometer results are obtained by finding the maximum electron number density in each array of cells along the normal to the surface. The electrostatic probe results are represented by the electron number density in the center of the last array of cells. A precise interpolation of the results to the correct position of the sensors was not required due to a negligible variation of the results between the last cell arrays.

The initial number of cells used was based on the ones used in recent works [7, 5, 3]. Along the wall, 160 cells are used, half of which are uniformly distributed on the circular nose, while the remaining ones are linearly growing along the cone. The number of cells in this direction is expected to have little influence on the results. On the direction normal to the surface, the mesh is initially generated with 80 cells with uniform spacing. A preliminary simulation was performed to roughly determine the shape and position of the shock. Then, the domain's upstream boundary is adjusted to reduce the area outside the shock layer and the cell size is adapted along the normal direction to cluster cells around the shock and in the boundary layer. The procedure used for this mesh adaptation is similar to the one found in the LAURA code [41].

To evaluate the quality of the mesh, the number of cells was doubled in the normal direction, while keeping the clustering previously done around the shock and boundary layer. Figure 4.9(a) shows the size of the cells along the stagnation streamline for the 80×160 mesh before and after mesh adaptation and mesh doubling. At the stagnation line, the cell size of the uniform mesh is 1.7×10^{-4} m. For the adapted mesh the minimum cell size is 9.7×10^{-5} m at the shock front and 2.3×10^{-5} m at the wall. The length of the cells along the wall is shown on figure 4.9(b), which is the same for the three cases, with a minimum of 2.7×10^{-3} m at the nose of the aircraft.

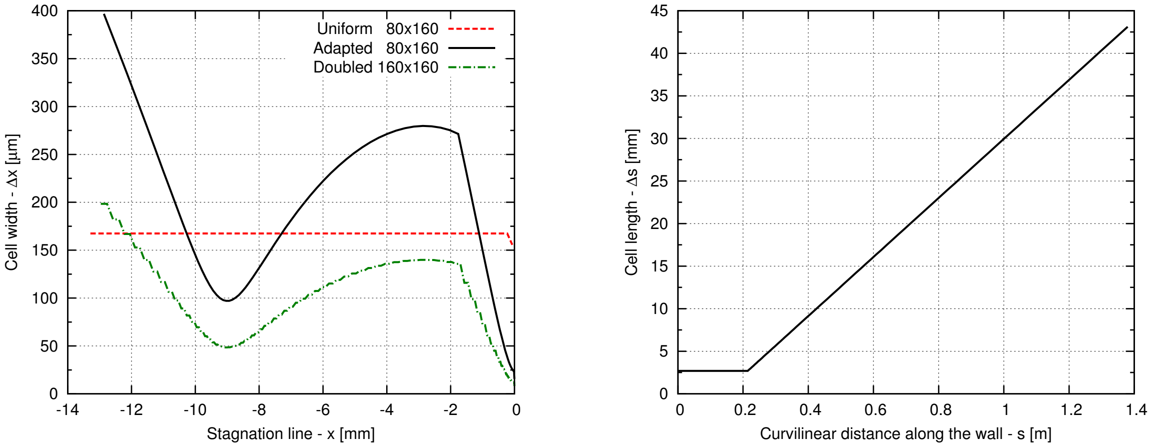

(a) Cell size along stagnation line

(b) Cell length along the wall

Figure 4.9: *Cell sizes for different meshes used*

The results presented in figure 4.10 were computed on these three meshes, using the Gupta-Yos/CCS transport model in thermal equilibrium. On the stagnation line temperature (fig. 4.10(a)) the precision improvement between the three meshes is very subtle, with a 1.3% variation in peak temperature after the mesh adaptation and 1.9% after doubling the number of cells, causing no relevant influence on the flow composition. However, for the heat flux at the wall (fig. 4.10(b)), the uniform mesh shows a 15% error relative to the adapted mesh. In turn, the difference between the adapted and the doubled mesh is only 0.03% at the maximum heating point with a maximum error of 2% towards the rear of the aircraft.

On the results for electron density, the difference of the maximum value along the body is about 20% between the uniform and the adapted mesh, and 10% relative to the doubled mesh. The results for the electron number as function of the distance from the wall show an increasingly large error although these values are already outside the zone of interest.

In conclusion, this analysis demonstrates that a grid of 80×160 cells is sufficient for the performed simulations. In particular, the mesh adaptation on the boundary layer proves to be very effective to accurately capture the strong gradients without increasing the computational cost.

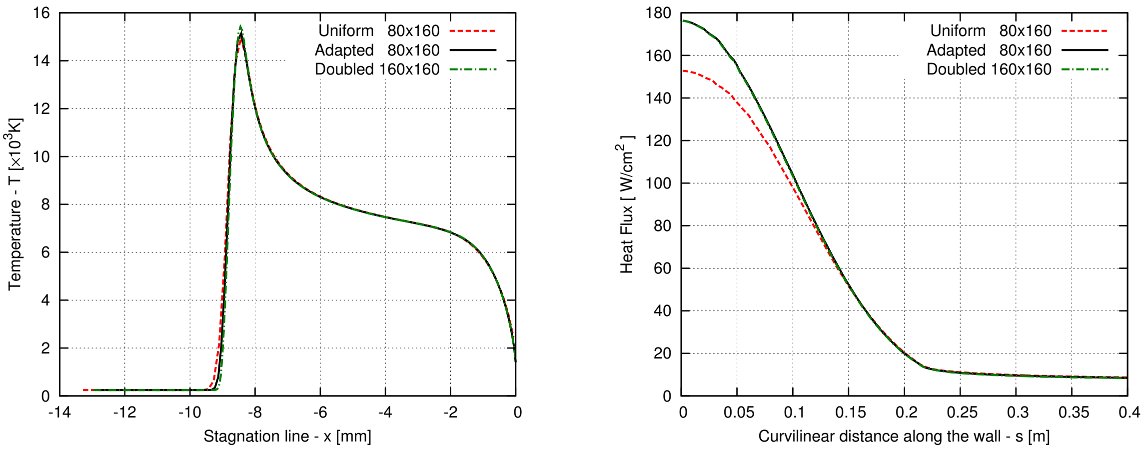

(a) Stagnation line Temperature

(b) Wall heat flux

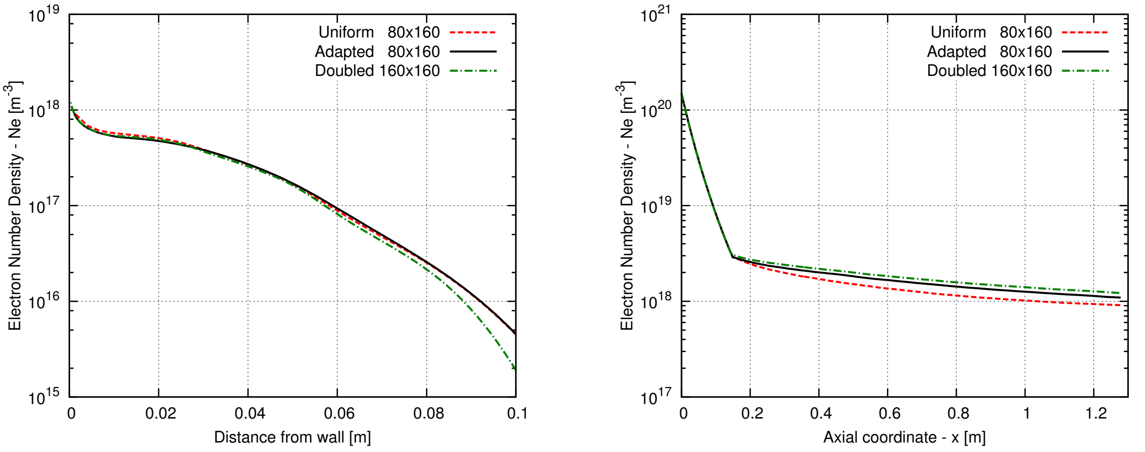

(c) Electron density along normal to wall (Electrostatic probe data)

(d) Electron density along body (Reflectometer data)

Figure 4.10: *Results for mesh convergence study of RAM-C II at 61km simulation*

4.2.3 Thermal equilibrium, Comparison of transport models

In figure 4.11, various results obtained for the 61km simulation in thermal equilibrium are plotted, for comparison and validation of the transport models, using the parameters and methods defined in sections 4.2.1 and 4.2.2.

In fig. 4.11(a) it can be seen that the effect of the transport model on the stagnation line temperature is negligible, causing a variation in the shock standoff distance in the order of $0.02\,\text{mm}$. The inviscid model causes a higher temperature at the shock and near the wall because no dissipation is being considered. Generally, the peak temperatures are within the expected order of magnitude, with $15 \times 10^3\,\text{K}$ for both transport models and $17 \times 10^3\,\text{K}$ for the inviscid.

The pressure inside the shock (fig. 4.11(b)) is also unaffected by the dissipation processes, although the shock front for the inviscid simulation shows a steeper gradient, possibly not properly captured by the mesh. This would explain the convergence difficulties encountered for this case. This shows that the introduction of dissipation processes, besides being more realistic, may help with the numerical stability, since they tend to alleviate strong discontinuities.

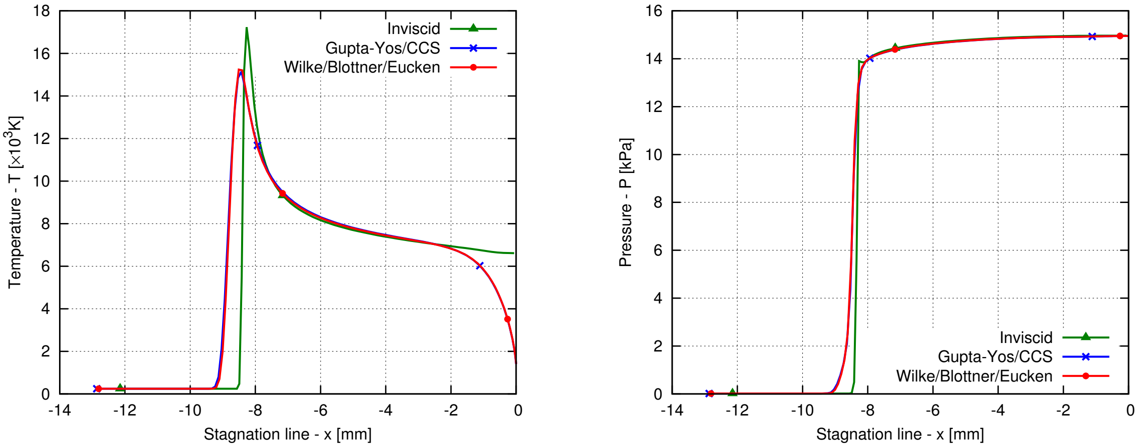

(a) Stagnation line Temperature

(b) Stagnation line Pressure

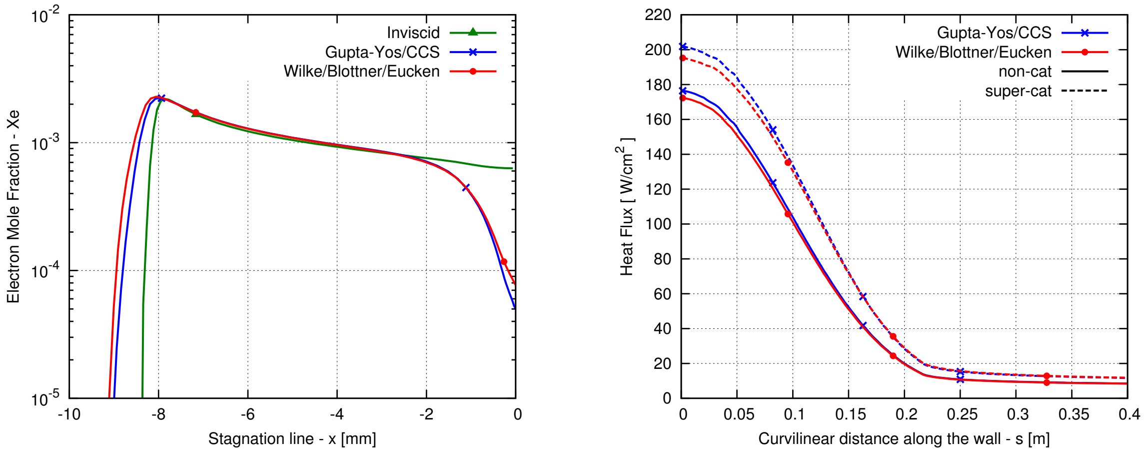

(c) Stagnation line Electron molar fraction

(d) Wall Heat flux

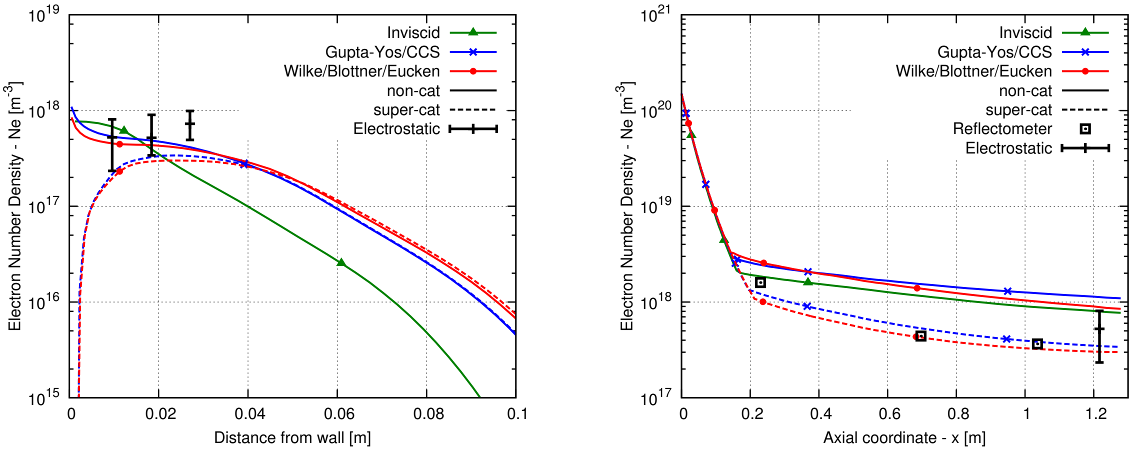

(e) Electron density along normal to wall and electrostatic robe data

(f) Electron density along body and microwave reflectometer data

Figure 4.11: *Comparison of transport models for the RAM-C II at 61km simulation in thermal equilibrium*

The electron mole fraction at the stagnation line (figure 4.11(c)) peaks below 3×10^{-3} , showing that the flow is weakly ionized and should generally be within the validity range of the approximate transport models, according to the observations in section 4.1.

The results for convective heat fluxes (fig. 4.11(d)) at the wall show that the influence of the transport model is negligible, causing a 2% variation in the stagnation point. However, when the super-catalytic boundary condition is used, an increase of 14% is obtained for the Gupta-Yos/CCS model and 13% for the Wilke/Blottner/Eucken model. It was also verified that the super-catalytic condition also causes the shock standoff distance to vary by approximately $0.1\,\mathrm{mm}$.

Figures 4.11(e) and 4.11(f) show again a relatively small influence on the chosen transport model, both cases showing a good correlation with the experimental data. The comparison with the inviscid case shows that the transport phenomena have a large influence on the electron density. As expected, the catalicity condition causes a large change in behavior for the curves near the wall. For the maximum electron density along the wall, the use of super-catalytic condition leads to a near perfect agreement with the experimental data for both models. It can also be inferred that the catalicity condition impacts the distance from the wall where the maximum electron density is found.

In general, all these results are sufficiently accurate for validating our implementation.

Figure 4.12 shows the chemical composition of the flow in the stagnation line obtained with the Gupta-Yos/CCS transport model with and without considering the *ambipolar* effect on the ions.

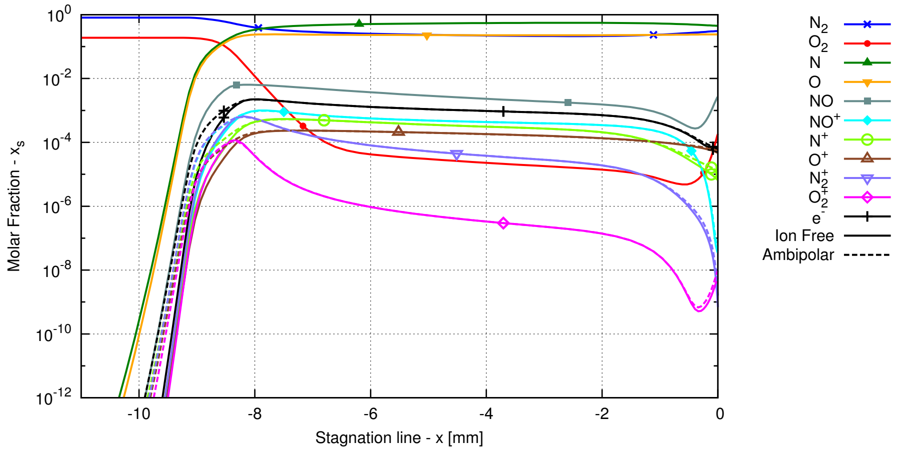

Figure 4.12: *Flow composition along stagnation line RAM-C II at 61km and ion ambipolar effect in thermal equilibrium*

As expected the *ambipolar* effect on the ions increases the diffusion of both ions and electrons. This is specially evident in the shock front, where the strong gradients cause the charged species to diffuse upstream of the shock front. Since thermal equilibrium is considered, this model is equivalent to a factor 2 increase in diffusion velocity. Therefore introducing the *ambipolar* effect does not necessarily lead to more accurate results.

Although not plotted, it was also observed that this effect does not have any significant improvement in the electron density results when compared with the experimental data.

4.2.4 Thermal non-equilibrium

The thermal non-equilibrium simulation results are plotted in figure 4.13. The thermal equilibrium results have been reported in dashed lines for comparison purposes.

Some results from the literature, which apply similar thermo-chemical models, are also reported in the figures.

All present results use the Gupta-Yos/CCS transport model, and a non-catalytic wall condition as well as the parameters and methods defined in sections 4.2.1 and 4.2.2.

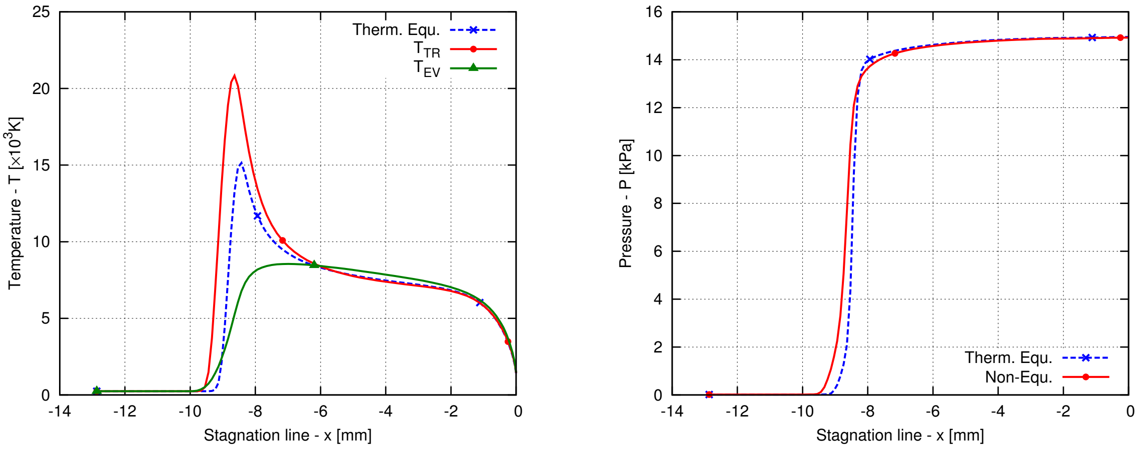

(a) Stagnation line Temperature

(b) Stagnation line Total Pressure

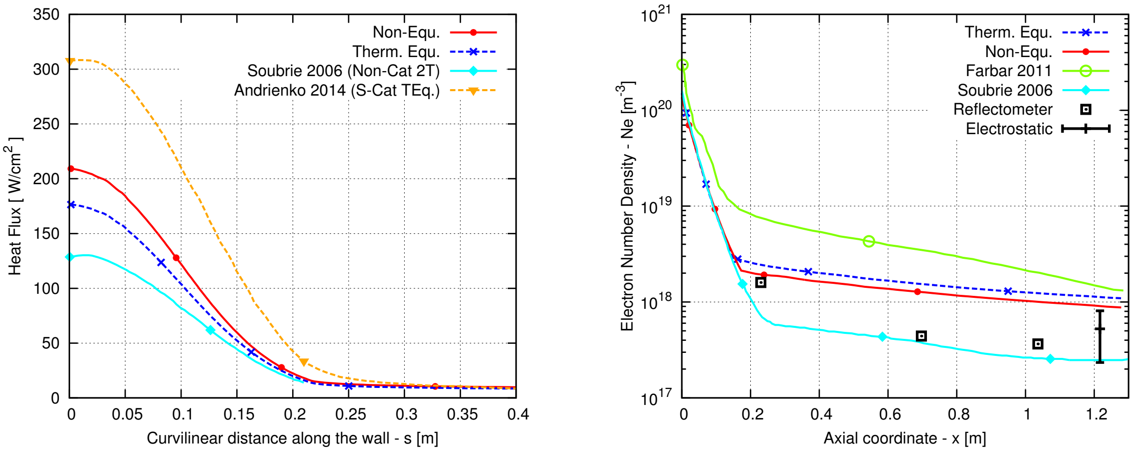

(c) Wall Heat Flux

(d) Electron density along body and microwave reflectometer data

Figure 4.13: *Thermal non-equilibrium results for the RAM-C II at 61km simulation using the Gupta-Yos/CCS model*

In the stagnation line temperature plot 4.13(a) it can be seen that the peak translational-rotational temperature, T_{TR}, is 40% higher if thermal non-equilibrium is considered. The electron-vibrational T_{EV} temperature is 60% smaller than T_{TR}, showing a very strong non-equilibrium as expected for this test case.

The thermal non-equlibrium also leads to a wider shock, with an increase in the shock standoff distance of $0.5\,\mathrm{mm}$. This can be observed in the pressure (fig. 4.13(b)), although this does not affect the total pressure inside the shock layer. This is expectable, since the pressure is not affected by the internal degrees of freedom of the particles.

Figure 4.13(c) shows that the non-equilibrium model leads to a 19% increase in the prediction of maximum convective heat fluxes at the wall. Comparison with other sources [6, 3] shows that the range of predictions for this result is very wide and sensitive to slight differences in the models and methods.

A comparison of the predicted electron density with the experimental (fig. 4.13(d)) data shows that there is a slight improvement of the results for the non-equilibrium simulation. Again, this results validate the implementation carried in this work, specially considering the variation introduced by the catalicity condition observed in thermal equilibrium (fig 4.11(f)). Nevertheless, a comparison with previous works [5, 6] shows a large discrepancy in the results, even though similar non-equilibrium models are used (Park 2001 [40] kinetics and two temperature thermal non-equilibrium, non-catalytic wall).

Fig, 4.14 shows the flow composition on the stagnation line, showing no relevant changes in comparison to the thermal equilibrium case (fig: 4.12), except for the effect of the wider shock front.

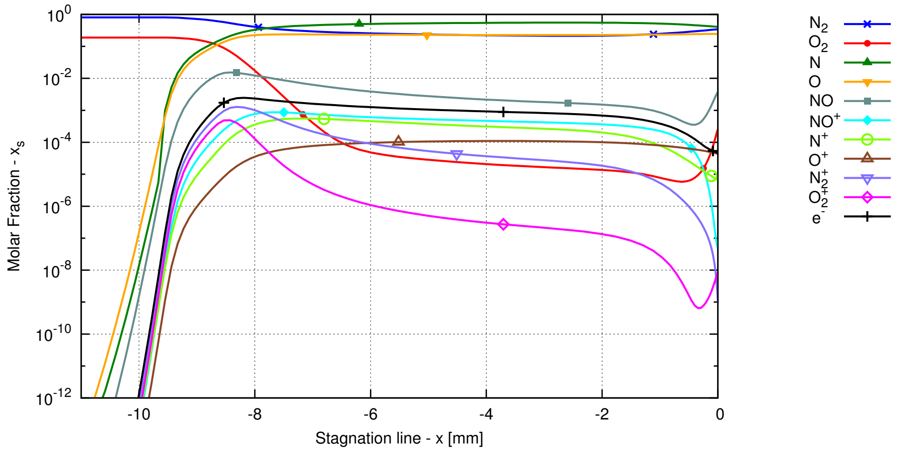

Figure 4.14: *Flow composition along stagnation line RAM-C II at 61km for a two temperature calculation*

4.3 Computational Cost

One of the advantages expected from the Wilke/Blottner/Eucken is a smaller computational cost than the Gupta-Yos/CCS, since the first does not require the computation of collision cross-sections for every pair or chemical species. The simplicity of the Eucken relation and the assumption of a constant Lewis number are also obviously less expensive than the more detailed mixing Gupta-Yos mixing rules for thermal conductivity and mass diffusion.

Nonetheless, studies have suggested that the use of the Gupta-Yos/CCS model may still be preferable, due to the smaller number of high-order mathematical operations required [14, 12]. Although, this advantage is minimal and is observed exclusivelly when only the viscosity coefficient is computed. In these studies, when the additional cost for computing thermal conductivity is considered, the cost of both models is shown to be very similar [12], or slightly more efficient with the Eucken model [17], as it would be expected.

In the present work, the computational cost of both models has been evaluated including the computation of the effective diffusion coefficients for the Gupta-Yos/CCS model. Both models also account for the internal specific heats and the shielding correction for the charged species (eq. (3.5)) which are also computationally expensive calculations. Therefore, this comparison represents a truly practical case for which all the transport properties are computed.

The computation cost has been evaluated by the CPU time required to perform different sets of repeated computations, ranging from 2000 to 10^7 points. It was consistently observed that for the current implementation, the Wilke/Blottner/Eucken uses about 50% of the CPU time of the Gupta-Yos/CCS model, effectively showing a great advantage in the selection of the simpler model.

However, it should be considered that in the context of a full simulation, the computation of the transport properties represents a very small portion of the computational cost of each iteration. By comparing the mean values ot the CPU time per iteration in full simulations, it was observed that Wilke/Blottner/Eucken is only 5 to 10 % quicker than the Gupta-Yos/CCS. Moreover, it was also generally observed that the use of the Gupta-Yos/CCS provided better solver stability and converged faster (i.e. in less iterations) than the Wilke/Blottner/Eucken model.

Chapter 5

Summary and Conclusions

Two approximate methods to compute the transport properties in hypersonic flows have been presented: the Wilke/Blottner/Eucken and the Gupta-Yos/CCS models.

While both are valid only for weakly ionized flows, the Gupta-Yos/CCS model is physically more accurate since less simplifications are taken in its derivation. The use of the Wilke/Blottner/Eucken model may still be advantageous, since it requires a smaller amount of input data, which may be more readily available.

A thorough investigation was done on the available models to compute the diffusion fluxes, while considering the *ambipolar* effect, i.e., the effect of the electrostatic forces between charged species on their diffusion velocity. It was observed that some of the more commonly used models were not necessarily valid for the present application, while others showed mathematical inconsistencies. Therefore an improved normalization method was proposed, for use in conjunction with the classic Fick Law, which introduces the *ambipolar* effect while ensuring the total mass conservation condition.

These models have been successfully implemented in the SPARK code, using an object-oriented *strategy* design pattern, which provides flexibility for the implementations of additional transport models in the future.

Some basic tests were performed for the detection of numerical problems, commonly related to mathematical singularities found in the applied models used. Solutions for removing such singularities have been discussed and implemented.

The implementation was validated by qualitative comparison of the viscosity and thermal conductivity coefficients with published data for the same models, and with exact multicomponent solutions for the equilibrium composition of air at the standard pressure.

This analysis has also shown that the Gupta-Yos/CCS model may return good results for higher ionization levels than the Wilke/Blottner/Eucken.

Although these results are satisfactory, improvements can be obtained by using a more up to date collision cross-section data set for the Gupta-Yos/CCS model, which can also be used to generate new curve fits for the Blottner model. The adjustment of the reciprocal Schmidt number may also improve the results of the Eucken model.

The code was applied to the simulation of the RAM-C II re-entry vehicle using both transport models, and experimental data from that flight experiment was used for additional validation and assessment of the results.

For the simulation in thermal equilibrium, both transport models provided excellent correlation with experimental data for electronic density, specially when considering wall catalicity.

The *ambipolar* effect on the diffusion of ions was verified on gas composition simulated on the stagnation line. It has observed that this does not introduce any relevant improvement on the results. Nonetheless the *ambipolar* diffusion effect on the electrons was effectively observed with this test, validating our implementation of the diffusion fluxes. A comparison of the electron diffusion coefficient computed with different models further justifies the method described in this work.

A simulation in thermal non-equilibrium was also successfully performed, with good correlation with experimental measurements. Numerical results found on the literature, applying similar non-equilibrium models show large discrepancies, specially for the convective heat flux. However, the values obtained here fall well within this range.

For the current implementation it was observed that the simple computation of the transport coefficients with Wilke/Blottner/Eucken model can be 50% faster than the Gupta-Yos/CCS. However, in the context of a full simulation, it was concluded that the use of the Gupta-Yos/CCS may actually be more efficient in some situations, due to improved numerical stability and faster convergence.

Given the similar overall numerical efficiency and the similarity of the simulation results it can be concluded that both models are equally recommendable for this particular test case. It should be stressed out that the Gupta-Yos/CCS model is more accurate for higher ionization levels, and will be more adequate for higher entry velocities (namely for super-orbital entries).

Bibliography

[1] John David Anderson. *Hypersonic and High Temperature Gas Dynamics*. AIAA, 1989.

[2] Jr. W. Linwood Jones and Aubrey E. Cross. Electrostatic-probe measurements of plasma parameters for two reentry flight experiments at 25 000 feet per second. Technical Report TN D-6617, NASA - Langley Reserach Center, 1972.

[3] Daniil A Andrienko. *Non-equilibrium Models for High Temperature Gas Flows*. PhD thesis, Wright State University, 2014.

[4] Iain D. Boyd. Modeling of associative ionization reactions in hypersonic rarefied flows. Technical report, Center for Turbulence Research, 2007.

[5] Erin Farbar, Iain D. Boyd, Minkwan Kim, and Alexandre Martin. Investigation of the Effects of Electron Translational Nonequilibrium on Numerical Predictions of Hypersonic Flow Fields. In *42nd AIAA Thermophysics Conference*, number 2011-3136, pages 1–20, Honolulu, Hawaii, 2011. AIAA.

[6] Tristan Soubrié. *Prise en compte de l'ionisation et du rayonnement dans la modélisation des écoulements de rentrée terrestre et martienne*. PhD thesis, L'École Nationale Supérieure de L'Aeronautique et de L'Espace, 2006.

[7] L. Walpot. *Development and application of a hypersonic flow solver*. PhD thesis, TUDelft, 2002.

[8] Eswar Josyula and William F. Bailey. Governing Equations for Weakly Ionized Plasma Flow fields of Aerospace Vehicles. *Journal of Spacecraft and Rockets*, 40(6):845–857, 2003.

[9] H Alkandry, Iain D. Boyd, and A Martin. Comparison of Models for Mixture Transport Properties for Numerical Simulations of Ablative Heat-Shields. In *51st AIAA Aerospace Sciences Meeting including the New Horizons Forum and Aerospace Exposition*, number 2013-0303, pages 1–18, Grapevine, Texas, 2013.

[10] Bruno Lopez. *Simulation des Écoulements de Plasma Hypersonique Hors Équilibre Thermochimique*. PhD thesis, Université D'Orléans, 2010.

[11] Sydney Chapman. The Mathematical Theory of Non-Uniform Gases, 1962.

[12] Thierry E. Magin and Gérard Degrez. Transport algorithms for partially ionized and unmagnetized plasmas. *Journal of Computational Physics*, 198:424–449, August 2004.

[13] C. R. Wilke. A Viscosity Equation for Gas Mixtures. *The Journal of Chemical Physics*, 18(4): 517–519, 1950.

[14] Grant E. Palmer and Michael J. Wright. Comparison of methods to compute high-temperature gas viscosity. *Journal of Thermophysics and Heat Transfer*, 17(2):232–239, 2003.

[15] Leonardo C Scalabrin. *Numerical simulation of weakly ionized hypersonic flow over reentry capsules*. PhD thesis, The University of Michigan, 2007.

[16] F. G. Blottner, M. Johnson, and M. Ellis. Chemically reacting viscous flow program for multi-component gas mixtures. Technical Report SC-RR-70-754, 1971.

[17] Grant E. Palmer and Michael J. Wright. A Comparison of Methods to Compute High-Temperature Gas Thermal Conductivity. In *36th AIAA Thermophysics Conference*, number 2003-3913, pages 1–16. AIAA, 2003.

[18] Roop N. Gupta, Jerrold M. Yos, Richard A. Thompson, and Kam-Pui Lee. A review of reaction rates and thermodynamic and transport properties for an 11-species air model for chemical and thermal nonequilibrium calculations to 30000 K. Technical Report RP 1232, NASA, 1990.

[19] Jerrold M. Yos. Approximate equations for the viscosity and translational thermal conductivity of gas mixtures. Technical Report Contract Report AVSSD-0112-67-RM, Avco Corporation, 1967.

[20] Kenneth Sutton and Peter A. Gnoffo. Multi-component Diffusion With Application to Computational Aerothermodynamics. In *7th AIAA/ASME Joint Thermophysics and Heat Transfer Conference*, number 98-2575, pages 1–14. AIAA, 1998.

[21] Jong-hun Lee. Basic Governing Equations For The Flight Regimes of Aeroassisted Orbital Transfer Vehicles. In *AIAA 19th Thermophysics Conference*, number 84-1729, pages 1–18, Snowmass, Colorado, 1984. AIAA.

[22] Peter A. Gnoffo, Roop N. Gupta, and Judy L. Shinn. Conservation Equations and Physical Models for Hypersonic Air Flows in Thermal and Chemical Nonequilibrium. Technical Report TP 2867, NASA, 1989.

[23] Georges Duffa. *Ablative Thermal Protection Systems Modeling*. AIAA, 2013.

[24] Robert J Kee, Graham Dixon-lewis, and James a Miller. A Fortran Computer Code Package For The Evaluation Of Gas-Phase Multicomponent Transport Properties. Technical Report SAND86-8246 UC-401, Sandia National Laboratories, 1986.

[25] Roop N. Gupta. Thermo-Chemical Nonequilibrium Analysis of Viscous Shock-Layers. In *30th AIAA Thermophysics Conference*, volume 95-2083, pages 1–27, San Diego, CA, 1995. AIAA.

[26] Francis F. Chen. *Introduction to Plasma Physics and Controlled Fusion Vol. 1*. Plenum Press, 2nd. edition, 1984.

[27] Tristan Soubrié, O. Rouzaud, and D. Zeitoun. Computation of weakly multi-ionized gases of atmospheric entry using an extended Roe scheme. In *European Congress on Computational Methods in Applied Science and Engineering*, number TP 2004-155, pages 1–19, Jyvaskyla, 2004.

[28] J. D. Ramshaw and C. H. Chang. Friction-Weighted Self-Consistent Effective Binary Diffusion Approximation. *Journal of Non-Equilibrium Thermodynamics*, 21:223–232, 1996.

[29] Damian Rouson, Jim Xia, and Xiaofeng Xu. *Scientific Software Design The Object-Oriented Way*. Cambridge, 2011.

[30] Michael J. Wright, Deepak Bose, Grant E. Palmer, and Eugene Levin. Recommended Collision Integrals for Transport Property Computations Part 1: Air Species. *AIAA Journal*, 43(12):2558–2564, 2005.

[31] R. A. Svehla. Estimated Viscosities and Thermal Conductivities of Gases at High Temperatures. Technical Report TR R-132, NASA Lewis Research Center, 1962.

[32] Sanford Gordon and Bonnie J. McBride. Computer Program for Calculation of Complex Chemical Equilibrium Compositions and Aplications. Technical Report RP 1311, NASA, 1994.

[33] Jerrold M. Yos. Transport properties of nitrogen, hydrogen, oxygen, and air to 30 000 K. Technical Report RAD-TM-63-7, Researche and Advanced Development Division - AVCO Corporation, Wilmington Massachusetts, 1963.

[34] Charles J Schexnayder, Jr. John S. Evans, and Paul W. Huber. Comparison of Theoretical and Experimental Electron Density for RAM C Flights. Technical report, NASA Langley Research Center, 1970.

[35] Chul Park. *Nonequilibrium Hypersonic Aerothermodynamics*. Wiley, New York, 1990.

[36] G. Candler. Translation-vibration-dissociation coupling in nonequilibrium hypersonic flows. *AIAA Paper*, (AIAA-89-1739), 1989.

[37] J.-H. Lee. Basic governing equations for the flight regimes of aeroassisted orbital transfer vehicles. *Progress in Astronautics and Aeronautics*, 96, 1985.

[38] R.C. Millikan and D.R. White. Systematics of Vibrational Relaxation. *Journal of Chemical Physics*, 39(12):3209–3213, 1963.

[39] J. P. Appleton, M. Steinberg, and D. J. Liquornik. No Title. *Journal of Chemical Physics*, 48:599–608, 1968.

[40] Chul Park, Richard L. Jaffe, and Harry Partridge. Chemical-Kinetic Parameters of Hyperbolic Earth Entry. *Journal of Thermophysics and Heat Transfer*, 15:76–90, 2001.

[41] F. McNeil Cheatwood and Peter a. Gnoffo. User's Manual for the Langley Aerothermodynamic Upwind Relaxation Algorithm (LAURA). Technical Report TM 4674, NASA, 1996.

Appendix A

Physical models

A.1 Thermodynamic Relations

A.1.1 Composition variables

The composition of the gas can be described by the number of particles of each chemical species contained in a volume of the gas. This defines the number density N_s (particles/m^3) and the molar density n_s (mol/m^3) of species s, with the two being related through the Avogadro constant N_{A}. Using these definitions, the global number density n and molar density N of the gas mixture can be determined by:

$$N = \sum_s N_s \qquad \text{and} \qquad n = \sum_s n_s \qquad \text{with:} \qquad n_s = \frac{N_s}{N_{\mathrm{A}}} \tag{A.1}$$

Knowing the species particle mass m_s (kg) or molar mass M_s (kg/mol), the mass density of each species ρ_s (kg/m^3) is defined as:

$$\rho_s = N_s m_s \qquad \text{or} \qquad \rho_s = n_s M_s \qquad \text{with:} \qquad m_s = \frac{M_s}{N_{\mathrm{A}}} \tag{A.2}$$

The mixture density ρ is given by:

$$\rho = \sum_s \rho_s \tag{A.3}$$

The previous quantities are used to define the species dimensionless composition variables mass fraction c_s and molar fraction x_s:

$$c_s = \frac{\rho_s}{\rho} \qquad \text{and} \qquad x_s = \frac{N_s}{N} = \frac{n_s}{n} \qquad \text{with:} \qquad \sum_s c_s = \sum_s x_s = 1 \tag{A.4}$$

The following relations can be used for conversion between the different composition variables:

$$x_s = \frac{M c_s}{M_s} \qquad n_s = \frac{x_s \rho}{M} \qquad c_s = \frac{n_s M_s}{\rho} \tag{A.5}$$

where M is the global mixture molar mass, which can be determined by:

$$M = \sum_s x_s M_s = \left(\sum_s \frac{c_s}{M_s} \right)^{-1} = \frac{1}{n} \sum_s n_s M_s \tag{A.6}$$

A.1.2 Equation of State

Considering that each chemical species in the mixture behaves as a ideal gas, the total pressure of the mixture P is defined by Dalton's Law as the summation of the partial pressures associated to each species P_s:

$$P = \sum_s P_s \tag{A.7}$$

the partial pressures are given by one of the various forms of the ideal gas equation of state:

$$P_s = \rho_s r_s T_{\mathrm{tra},s} \qquad \text{or} \qquad P_s = N_s k_{\mathrm{B}} T_{\mathrm{tra},s} \qquad \text{or} \qquad P_s = n_s R_{\mathrm{u}} T_{\mathrm{tra},s} \tag{A.8}$$

where r_s is the specific gas constant for the species s, k_{B} is the Boltzmann constant and R_{u} is the universal gas constant, which can be related by:

$$r_s = \frac{R_{\mathrm{u}}}{M_s} = \frac{k_{\mathrm{B}}}{m_s} \qquad \text{and} \qquad k_{\mathrm{B}} = \frac{R_{\mathrm{u}}}{N_{\mathrm{A}}} \tag{A.9}$$

Generally, in thermal non-equilibrium, the global pressure P is a function of all the translational temperatures associated with each chemical species $T_{\mathrm{tra},s}$. Assuming that all the heavy species have the same translational temperature T_{h}, which can be different from the electronic temperature T_{e}, we can write the total pressure as:

$$P = P_{\mathrm{h}} + P_{\mathrm{e}} \tag{A.10}$$

where the heavy pressure P_{h} and electronic pressure P_{e} are given by:

$$\begin{cases} P_{\mathrm{h}} & = \rho R_{\mathrm{h}} T_{\mathrm{h}} \\ P_{\mathrm{e}} & = \rho R_{\mathrm{e}} T_{\mathrm{e}} \end{cases} \qquad \text{with:} \qquad \begin{cases} R_{\mathrm{h}} & = \sum\limits_{s=\mathrm{h}} c_s r_s \\ R_{\mathrm{e}} & = c_{\mathrm{e}} r_{\mathrm{e}} \end{cases} \tag{A.11}$$

The global gas constant is given by

$$R = \sum_{s=\mathrm{h}} c_s r_s = R_{\mathrm{h}} + R_{\mathrm{e}} = \frac{R_{\mathrm{u}}}{M} \tag{A.12}$$

which, in the case of electronic thermal equilibrium ($T_{\mathrm{h}} = T_{\mathrm{e}} = T$), can be used to define the total pressure as:

$$P = \rho R T \tag{A.13}$$

A.1.3 Internal energy

The specific internal energy of gas ε represents the total energy stored in the internal degrees of freedom of its particles and also in their chemical bonds, per unit of mass. It is defined as function of the contributions of each chemical species ε_s and their corresponding mass fraction c_s:

$$\varepsilon = \sum_s c_s \varepsilon_s \tag{A.14}$$

The internal energy associated to each chemical species ε_s is defined by:

$$\varepsilon_s = \Delta h_s^\circ + \varepsilon_{\mathrm{tra},s} + \varepsilon_{\mathrm{rot},s} + \varepsilon_{\mathrm{vib},s} + \varepsilon_{\mathrm{exc},s} \tag{A.15}$$

The term Δh_s° is the standard formation enthalpy, and the terms $\varepsilon_{\mathrm{tra},s}$, $\varepsilon_{\mathrm{rot},s}$, $\varepsilon_{\mathrm{vib},s}$, $\varepsilon_{\mathrm{exc},s}$ correspond to the different of thermal energy modes $\varepsilon_{k,s}$ associated with each species as described in the multi-temperature model, section 2.1.2.

As a result of quantum physics, the thermal energy of a particle is defined by discrete energy levels (states) for each degree of freedom. The amount of energy $\varepsilon_{k,s}$ generally stored in each energy mode k for a given chemical species s can be defined statistically as function of the corresponding temperature $T_{k,s}$ by Maxwell-Boltzmann distributions [1] :

$$\varepsilon_{\mathrm{tra},s} = r_s T_{\mathrm{tra},s} \frac{3}{2} \tag{A.16a}$$

$$\varepsilon_{\mathrm{rot},s} = r_s T_{\mathrm{rot},s} \tag{A.16b}$$

$$\varepsilon_{\mathrm{vib},s} = r_s \frac{\theta_{\mathrm{vib},s}}{\exp\left(\dfrac{\theta_{\mathrm{vib},s}}{T_{\mathrm{vib},s}}\right) - 1} \tag{A.16c}$$

$$\varepsilon_{\mathrm{exc},s} = r_s \frac{\displaystyle\sum_i^\infty \theta_{\mathrm{exc},i,s}\, g_{i,s}\, \exp\left(-\frac{\theta_{\mathrm{exc},i,s}}{T_{\mathrm{exc},s}}\right)}{\displaystyle\sum_i^\infty g_{i,s}\, \exp\left(-\frac{\theta_{\mathrm{exc},i,s}}{T_{\mathrm{exc},s}}\right)} \tag{A.16d}$$

where $\theta_{\mathrm{vib},s}$ is the species characteristic vibrational temperature, $\theta_{\mathrm{exc},i,s}$ is the characteristic electronic temperature and and $g_{i,s}$ is the degeneracy of the i-th energy level of the species. The ∞ symbol represents the highest achievable energy level before ionization, although, in practice, a finite number of electronic levels may be considered, according to the order of magnitude of the energy exchanges present in the flow. In this work only the electronic levels below $10\,\mathrm{eV}$ have been considered, which should suffice to model any earth reentry. The equations for the rotational $\varepsilon_{\mathrm{rot},s}$ and vibrational $\varepsilon_{\mathrm{vib},s}$ modes apply only to the particular case of diatomic molecules.

If thermal non-equilibrium is considered, the global internal energy ε_k associated to each global temperature T_k of the mixture is given by:

$$\varepsilon_k = \sum_s c_s \varepsilon_{k,s} \tag{A.17}$$

where each global thermal energy mode ε_k depends only on the temperature T_k. The total internal energy of the mixture ε can then be calculated, equivalently to equation (A.14) with dependence on all temperatures, by:

$$\varepsilon = \Delta h^\circ + \sum_k \varepsilon_k \qquad \text{with:} \qquad \Delta h^\circ = \sum_s c_s \Delta h_s^\circ \tag{A.18}$$

Enthalpy

From its definition, the specific enthalpy h of the gas is given by:

$$h = \varepsilon + \frac{P}{\rho} \tag{A.19}$$

which can be generalized for the multi component and case as, similarly to equations (A.14) and (A.15) as:

$$h = \sum_s c_s h_s \tag{A.20}$$

$$h_s = \varepsilon_s + \frac{P_s}{\rho_s} \qquad \text{or} \qquad h_s = \varepsilon_s + r_s T_{\text{tra},s} \tag{A.21}$$

and also considering the different internal energy modes:

$$h_s = \Delta h_s^\circ + h_{\text{tra},s} + h_{\text{rot},s} + h_{\text{vib},s} + h_{\text{exc},s} \qquad \text{with:} \qquad \begin{cases} h_{\text{tra},s} & = \varepsilon_{\text{tra},s} + r_s T_{\text{tra},s} \\ h_{\text{rot},s} & = \varepsilon_{\text{rot},s} \\ h_{\text{vib},s} & = \varepsilon_{\text{vib},s} \\ h_{\text{exc},s} & = \varepsilon_{\text{exc},s} \end{cases} \tag{A.22}$$

The component $r_s T_{\text{tra},s}$ is only considered in the translational enthalpy since the the translational motion associated to $T_{\text{tra},s}$ is the microscopic mechanism responsible for pressure force.

The global enthalpy h_k associated to each temperature T_k is given by:

$$h_k = \sum_s c_s h_{k,s} \tag{A.23}$$

and the total enthalpy of the mixture h can also be calculated by:

$$h = \Delta h^\circ + \sum_k h_k \tag{A.24}$$

Specific Heats

The gas specific heat at constant volume C_{V} and the specific heat at constant pressure C_{P} are defined as the rate of change as a function of the temperature for the internal energy and enthalpy respectively:

$$C_{\mathrm{V}} \equiv \frac{\partial \varepsilon}{\partial T} \qquad \text{and} \qquad C_{\mathrm{P}} \equiv \frac{\partial h}{\partial T} \tag{A.25}$$

In the multi-temperature approach, the previous definitions become:

$$\begin{cases} C_{\mathrm{V}k} &= \dfrac{\partial \varepsilon_k}{\partial T_k} \\ C_{\mathrm{P}k} &= \dfrac{\partial h_k}{\partial T_k} \end{cases} \qquad \text{and} \qquad \begin{cases} C_{\mathrm{V}} &= \displaystyle\sum_k C_{\mathrm{V}k} \\ C_{\mathrm{P}} &= \displaystyle\sum_k C_{\mathrm{P}k} \end{cases} \tag{A.26}$$

Introducing equations (A.17) and (A.23) into equation (A.26) we obtain:

$$\begin{cases} C_{\mathrm{V}k} &= \displaystyle\sum_s \left(c_s \frac{\partial \varepsilon_{k,s}}{\partial T_{k,s}} + \varepsilon_{k,s} \frac{\partial c_s}{\partial T_{k,s}} \right) \\ C_{\mathrm{P}k} &= \displaystyle\sum_s \left(c_s \frac{\partial h_{k,s}}{\partial T_{k,s}} + h_{k,s} \frac{\partial c_s}{\partial T_{k,s}} \right) \end{cases} \tag{A.27}$$

In this equation, we can identify a frozen component, i.e., the specific heats considering a constant chemical composition of the gas, and a reactive component, associated with the heat exchange due to the chemical reactions. The global frozen specific heats at constant volume $C_{\mathrm{V}}{}^{\mathrm{f}}_{k}$ and at constant pressure $C_{\mathrm{P}}{}^{\mathrm{f}}_{k}$, of associated to each temperature T_k are defined as:

$$\begin{cases} C_{\mathrm{V}}{}^{\mathrm{f}}_{k} = \displaystyle\sum_s c_s C_{\mathrm{V}}{}^{\mathrm{f}}_{k,s} \\ C_{\mathrm{P}}{}^{\mathrm{f}}_{k} = \displaystyle\sum_s c_s C_{\mathrm{P}}{}^{\mathrm{f}}_{k,s} \end{cases} \qquad \text{with:} \qquad \begin{cases} C_{\mathrm{V}}{}^{\mathrm{f}}_{k,s} = \dfrac{\partial \varepsilon_{k,s}}{\partial T_{k,s}} \\ C_{\mathrm{P}}{}^{\mathrm{f}}_{k,s} = \dfrac{\partial h_{k,s}}{\partial T_{k,s}} \end{cases} \tag{A.28}$$

Throughout this work only the frozen component of the specific heat coefficients are used, without any approximation. For simplicity the symbols C_{V} and C_{P} are used to refer to the frozen components. Using the frozen definitions, and equations (A.22) and (A.16) the specific heats associated to the internal energy modes of each chemical species are given by:

$$\begin{cases} C_{\mathrm{V}\,\mathrm{tra},s} &= \dfrac{3}{2} r_s \qquad ; \qquad C_{\mathrm{P}\,\mathrm{tra},s} = \dfrac{5}{2} r_s \\ C_{\mathrm{V}\,\mathrm{rot},s} &= C_{\mathrm{P}\,\mathrm{rot},s} = r_s \\ C_{\mathrm{V}\,\mathrm{vib},s} &= C_{\mathrm{P}\,\mathrm{vib},s} = \dfrac{\partial \varepsilon_{\mathrm{vib},s}}{\partial T_{\mathrm{vib},s}} \\ C_{\mathrm{V}\,\mathrm{exc},s} &= C_{\mathrm{P}\,\mathrm{exc},s} = \dfrac{\partial \varepsilon_{\mathrm{exc},s}}{\partial T_{\mathrm{exc},s}} \end{cases} \tag{A.29}$$

The specific heats relate to the global R and species r_s gas constants and the specific heat ratio γ by:

$$R = C_{\mathrm{P}} - C_{\mathrm{V}} \quad , \quad r_s = C_{\mathrm{P}\,\mathrm{tra},s} - C_{\mathrm{V}\,\mathrm{tra},s} \qquad \text{and} \qquad \gamma = \frac{C_{\mathrm{P}}}{C_{\mathrm{V}}} \tag{A.30}$$

A.2 Multi-temperature models

The most commonly used models are presented in table A.1, establishing the correspondence between the temperatures associated to the species thermal energy modes $\varepsilon_{k,s}(T_{k,s})$ and the global temperatures T_k considered:

Table A.1: *Multi-temperature models*

$T_{k,s} \to T_k$	k=tra		k=rot	k=vib	k=exc
	s=e	s=h	s=m	s=m	s=h
a) $N.T. = 1$	T	T	T	T	T
b) $N.T. = 2$	T_{VE}	T_{TR}	T_{TR}	T_{VE}	T_{VE}
c) $N.T. = 3$	T_{e}	T_{TR}	T_{TR}	T_{VE}	T_{VE}
d) $N.T. = 3$	T_{Ee}	T_{TR}	T_{TR}	T_{V}	T_{Ee}
e) $N.T. = 2 + \mathrm{N}_{\mathrm{V}s}$	T_{Ee}	T_{TR}	T_{TR}	T_{V_s}	T_{Ee}

a) The first approximation corresponds to the assumption of thermal equilibrium, with $T_{k,s} = T$.

b) Generally, there is always an equilibrium between the translational and rotational modes of heavy species $T_{\mathrm{tra,h}} = T_{\mathrm{rot,h}}$ since the two equilibrate in just a few collisions, defining the translational-rotational global temperature T_{TR}. Because of a great difference in mass, the translational energy of free electrons can be significantly different from the energy of heavy particles. Since the interaction of free electrons with vibrational mode of molecules and with bounded electrons on the electronic levels of particles is very efficient, it is often assumed that the these tree modes are in equilibrium at the vibration-electronic-electron temperature T_{VE}. This type of non-equilibrium is the two temperature model, proposed by Park [35] and has been used in several works [25, 22, 15].

c) Some studies such as Farbar et al. [5], show that the non-equilibrium between the free electron translational mode and the vibrational mode of the heavy species may be significant, therefore introducing a third non-equilibrium temperature $T_{\mathrm{tra,e}} \equiv T_{\mathrm{e}}$. In this work the electronic excitation was considered in equilibrium with the vibrational mode of the heavy species at T_{VE}. d) Although it is also common [22, 3] to consider a independent vibrational temperature T_{V} while the electronic excitation mode is in equilibrium with the translational of free electrons, defining the electron-electronic temperature T_{Ee}. Other works [27] simplify by completely neglecting the effect of the electronic excitation.

e) The next step is to consider the vibrational temperature of each chemical species independently T_{V_s}, since the vibrational energy depends on the characteristic frequency of the molecular bonds and, thus, is different for individual types of molecules. This approach has been used in the works of Soubrié [27] and Andrienko [3].

A.3 Conservation Equations

The flow is modeled by a system of partial differential equations, which can be formulated in a generic form for the dependent variable ϕ:

$$\underbrace{\frac{\partial}{\partial t}(\rho\phi)}_{\text{transient}} + \underbrace{\vec{\nabla}\cdot(\rho\phi\vec{u})}_{\text{advective}} = \underbrace{\vec{\nabla}\cdot\vec{J_\phi}}_{\text{diffusive}} + \underbrace{S_\phi}_{\text{source}} \tag{A.31}$$

where $\vec{u}$ is macroscopic velocity field vector and ρ is the global gas density.

The complete system represents an extension of the classical Navier-Stokes equations, implying a continuum flow ($\mathrm{Kn} < 0.01$). It comprises one mass conservation equation per chemical species considered, one momentum conservation equation per spacial dimension and one total energy conservation equation. Additionally one thermal energy conservation equation is considered per non-equilibrium temperature considered. The terms of each equation are summarized in table A.2.

Table A.2: *List of conservation equation variables and dimensions in S.I. units*

Conservative Qty.		Dependent var		Flux		Source	
$\rho\phi\Delta V$	Φ	ϕ	Φ·kg^{-1}	$\vec{J_\phi}$	Φ·m^{-2}·s^{-1}	S_ϕ	Φ·m^{-3}·s^{-1}
Mass of species s	kg	c_s	$-$	$\vec{J_s}$	kg·m^{-2}·s^{-1}	$\dot{\omega}_s$	kg·m^{-3}·s^{-1}
Momentum	N·s	$\vec{u}$	m·s^{-1}	$[\sigma]$	N·m^{-2}	$\vec{f}$	N·m^{-3}
Total energy	J	E	J·kg^{-1}	$\vec{q}_E$	J·m^{-2}·s^{-1}	$\dot{Q}$	J·s^{-1}·m^{-3}
Thermal energy k	J	ε_k	J·kg^{-1}	$\vec{q}_k$	J·m^{-2}·s^{-1}	$\dot{\Omega}_k$	J·s^{-1}·m^{-3}

Mass conservation

The mass conservation equations control the chemical composition of the gas, which is defined by the mass fraction of each species $c_s = \rho_s/\rho$ as dependent variable.

The mass diffusion flux $\vec{J_s}$ represents the rate mass of species s entering the CV due to mean Brownian movement of the particles in the presence of concentration gradients. Generally, it is modeled by Fick's Law of diffusion:

$$\vec{J_s} = \rho D_s \vec{\nabla}(c_s) \tag{A.32}$$

where D_s is the diffusion coefficient of species s and $D_s\vec{\nabla}(c_s)$ is the corresponding diffusion velocity, which can be interpreted as the deviation of the velocity of species s from the mean global velocity $\vec{u}$. Although, the application of this model in a weakly ionized multi-component gas requires further analysis, which is done in section 2.3.

The source term $\dot{\omega}_s$ is the rate of creation of species s due to chemical reactions, derived from chemical-kinetics theory.

The concrete formulation of the equation for each species is:

$$\frac{\partial}{\partial t}(\rho c_s) + \vec{\nabla}\cdot(\rho\vec{u}c_s) = \vec{\nabla}\cdot\vec{J_s} + \dot{\omega}_s \tag{A.33}$$

Although this equation implies that the total mass of a given species on the system may change, the total mass of the mixture must always be conserved, as stated by the continuity equation:

$$\frac{\partial \rho}{\partial t} + \vec{\nabla} \cdot (\rho \vec{u}) = 0 \tag{A.34}$$

This result can be obtained by the summation of the $\mathrm{N}s$ equations of species mass conservation, while ensuring that:

$$\sum_s \vec{J}_s = 0 \tag{A.35}$$

and

$$\sum_s \dot{\omega}_s = 0 \tag{A.36}$$

In this model only the diffusion due to concentration gradients is considered, although, there would also be an effect of pressure and thermal diffusion, due to gradients of the total pressure $\vec{\nabla} P$ and temperature $\vec{\nabla} T$, respectively. These effects have not been considered since they are relatively small compared to mass diffusion [1].

Momentum conservation

The momentum conservation equation, results from the application of Newton's second law to the fluids motion, with the applied resultant force density being represented by the diffusive and source terms.

In the diffusive term, the momentum flux $[\sigma]$ is the stress tensor which includes the effects of pressure and viscosity:

$$[\sigma] = [\tau] - P\,[\mathrm{I}] \tag{A.37}$$

where $[\tau]$ is the viscous stress tensor, P is the total pressure and $[\mathrm{I}]$ is the identity matrix. The negative sign on the pressure component is due to the fact that the pressure acts in the opposite direction to its gradient.

The viscous stress tensor $[\tau]$ is a function of the velocity gradient $\nabla \vec{u}$, assuming a Newtonian fluid and the Stokes hypothesis for the normal stresses:

$$[\tau] = \mu \left(\vec{\nabla} \vec{u} + (\vec{\nabla} \vec{u})^{\mathsf{T}} \right) - \frac{3}{2} \mu (\vec{\nabla} \cdot \vec{u})\,[\mathrm{I}] \tag{A.38}$$

where μ is the gas viscosity coefficient, detailed in section 2.2

The source term $\vec{f}$ represents the force density caused by any external force fields, commonly the gravitational ($\rho \vec{g}$) or electro-magnetic forces, although they are not considered in the current application, consequently $\vec{f} = 0$.

With these definitions, the concrete formulation of the equation is[1]:

$$\frac{\partial}{\partial t} (\rho \vec{u}) + \vec{\nabla} \cdot (\rho \vec{u} \otimes \vec{u}) = \vec{\nabla} \cdot [\tau] - \vec{\nabla} P + \vec{f} \tag{A.39}$$

---

[1] The terms of this equation are given in vectorial form, with each vectorial component representing the momentum conservation in one spacial dimension. The operator $\otimes$ is the tensor product.

In this formulation, it was assumed that the gas moves as a whole with a global velocity $\vec{u}$. Yet in an accurate multi-species model, each species may have a different velocity $\vec{u}_s$, implying one vectorial momentum equation for each one. The consideration of only one global flow velocity is very advantageous from a computational point of view, and is a perfectly valid approximation due to the similarity of the species mass. Although, it may loose validity when ionization occurs, due to the introduction of electrons with a large mass discrepancy, and the acceleration of the charged species in the presence of electric fields [10]. Yet this effect is mitigated by the *ambipolar* effect detailed in section 2.3.

Total Energy conservation

In the total energy conservation equation, the dependent var E is the specific total energy, which includes the global specific internal energy ε (eq. (A.14)) and the kinetic energy of the flow, per unit of mass:

$$E = \varepsilon + \frac{\vec{u} \cdot \vec{u}}{2} \tag{A.40}$$

The total energy flux $\vec{q_E}$ accounts for all the global energy dissipation processes and is given by:

$$\vec{q_E} = \vec{q_\mathrm{C}} + \vec{q_\mathrm{D}} + \vec{q_\sigma} \tag{A.41}$$

The first contribution $\vec{q_\mathrm{C}}$ is the heat dissipation through conduction, due to temperature gradients, comprising all the contributions of the global non-equilibrium temperatures K considered:

$$\vec{q_\mathrm{C}} = \sum_k \vec{q_\mathrm{C}}_k \tag{A.42}$$

where the heat conducted in each non-equilibrium temperature mode $\vec{q_\mathrm{C}}_k$ is given by Fourier's Law of heat conduction, with the thermal conductivity coefficient λ_k:

$$\vec{q_\mathrm{C}}_k = \lambda_k \vec{\nabla} T_k \tag{A.43}$$

The term $\vec{q_\mathrm{D}}$ is the dissipation of enthalpy associated to the mass diffusion flux $\vec{J_s}$ of each chemical species:

$$\vec{q_\mathrm{D}} = \sum_s \vec{J_s} h_s \tag{A.44}$$

where the species enthalpy h_s is given by equation (A.22). Finally, $\vec{q_\sigma}$ is the heat dissipated through the work done by the stress tensor (eq. (A.37)).

$$\vec{q_\sigma} = \vec{u} \cdot [\sigma] = \vec{u} \cdot [\tau] - P\vec{u} \tag{A.45}$$

The source term $\dot{Q}$ represents the radiant energy transfer rate due to electronic transitions $\dot{Q}_R$ and also other possible effects such as Joule effect heating. The radiation term $\dot{Q}_R$ may have an important contribution in high temperature flows, although it has not been considered, since it requires specialized quantum-mechanical models which are commonly decoupled from the multi-temperature Navier-Stokes formulation.

The final form of the total energy conservation is:

$$\frac{\partial}{\partial t}(\rho E) + \vec{\nabla} \cdot (\rho \vec{u} E) = \vec{\nabla} \cdot \left(\sum_k \vec{q_{\mathrm{C}}}_k + \sum_s \vec{J}_s h_s + \vec{u} \cdot [\tau] - P\vec{u} \right) + \dot{Q} \tag{A.46}$$

Non-equilibrium Thermal Energy Conservation

When thermal non-equilibriums are considered, one energy conservation needs to be considered for each additional non-equilibrium temperature.

The terms in the equation depend on the type of non-equilibriums considered, although a general form can be presented, which applies for any of the global temperature modes presented in table A.1.

The dependent variable is the global thermal energy ε_k associated to the temperature T_k, given by equation (A.17). On the advective term the corresponding enthalpy h_k is used, as defined by eq. (A.23), to introduce the pressure term, $P_s \vec{\nabla} \cdot \vec{u}$, if the any translational mode is considered (commonly only the electron), being otherwise equivalent to using ε_k. The flux term comprises conduction and diffusion contributions: $\vec{q}_k = \vec{q_{\mathrm{C}}}_k + \vec{q_{\mathrm{D}}}_k$. The general form of the non equilibrium equations is then:

$$\frac{\partial}{\partial t}(\rho \varepsilon_k) + \vec{\nabla} \cdot (\rho \vec{u} h_k) = \vec{\nabla} \cdot (\vec{q_{\mathrm{C}}}_k + \vec{q_{\mathrm{D}}}_k) + \dot{\Omega}_k \tag{A.47}$$

where conduction heat flux $\vec{q_{\mathrm{C}}}_k$ term is given by equation (A.43), and the diffusion heat flux $\vec{q_{\mathrm{D}}}_k$ can be defined by:

$$\vec{q_{\mathrm{D}}}_k = \sum_s \vec{J}_s h_{s,k} \tag{A.48}$$

The source term $\dot{\Omega}_k$ represents the coupling between the different energy equations, given by the relaxation models, depending on the multi-temperature considered. It may also include dependencies on the chemical-kinetics and electrostatic interactions between charged species, as well as a radiation term $\dot{Q}_{Rk}$ if considered. The formulation of this term is out of the scope of this work.

Appendix B

Data Plots

B.1 Collision Cross-Sections

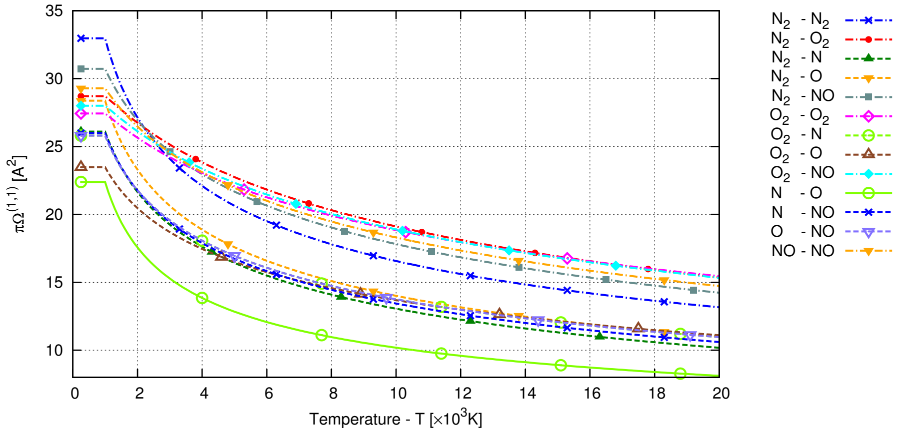

(a) Diffusion collision cross-sections $\pi\overline{\Omega}^{(1,1)}_{sr}$ for interactions between neutral species. The curves for $\mathrm{O}-\mathrm{O}$ and $\mathrm{N}-\mathrm{N}$ were omitted, since they are the same as $\mathrm{O}^{+}-\mathrm{O}$ and $\mathrm{N}^{+}-\mathrm{N}$ respectively, which be found in fig B.2(a).

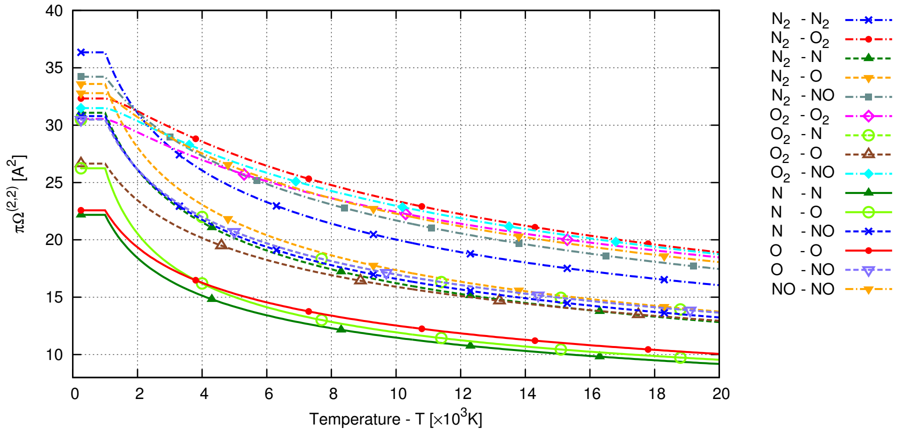

(b) Viscosity collision cross-sections $\pi\overline{\Omega}^{(2,2)}_{sr}$ for interactions between neutral species

Figure B.1: *Collision cross-sections as function of temperature, neutral species*

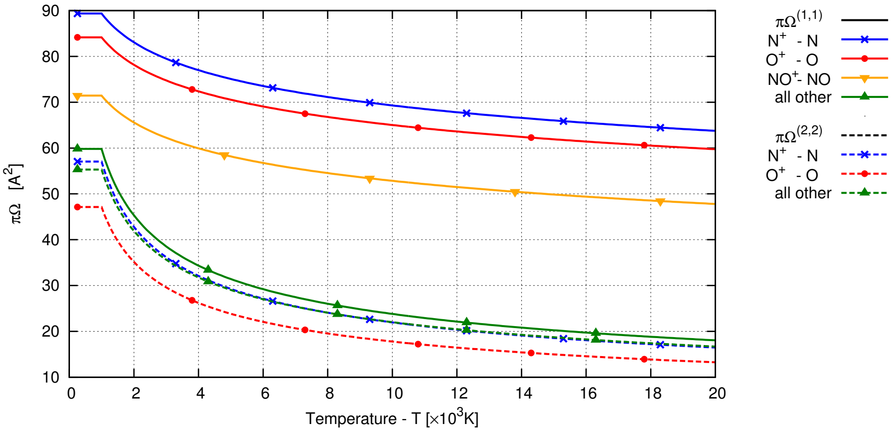

(a) Collision cross-sections ($\pi\overline{\Omega}_{sr}^{(1,1)}$ and $\pi\overline{\Omega}_{sr}^{(2,2)}$) for interactions between ions and neutral species

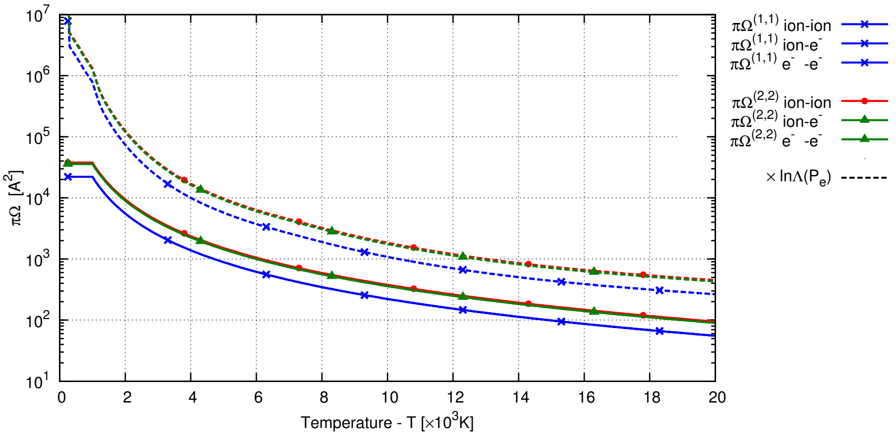

(b) Collision cross-sections ($\pi\overline{\Omega}_{sr}^{(1,1)}$ and $\pi\overline{\Omega}_{sr}^{(2,2)}$) for interactions between charged species, with shielding effect correction $(\ln \Lambda(P_{\mathrm{e}}))$ for equilibrium air 1 atm

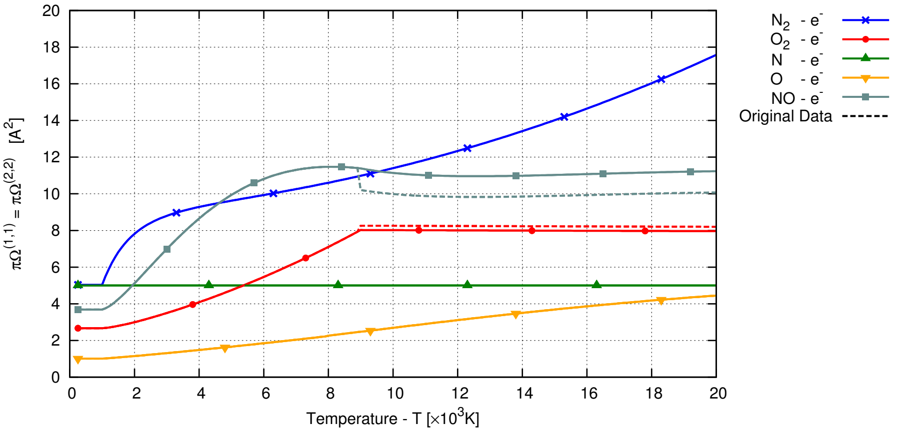

(c) Collision cross-sections ($\pi\overline{\Omega}_{sr}^{(1,1)} = \pi\overline{\Omega}_{sr}^{(2,2)}$) for interactions between electrons and neutral species, with discontinuity correction and also original data from ref. [18]

Figure B.2: *Collision cross-sections as function of temperature, charged species*

B.2 Viscosity Coefficients

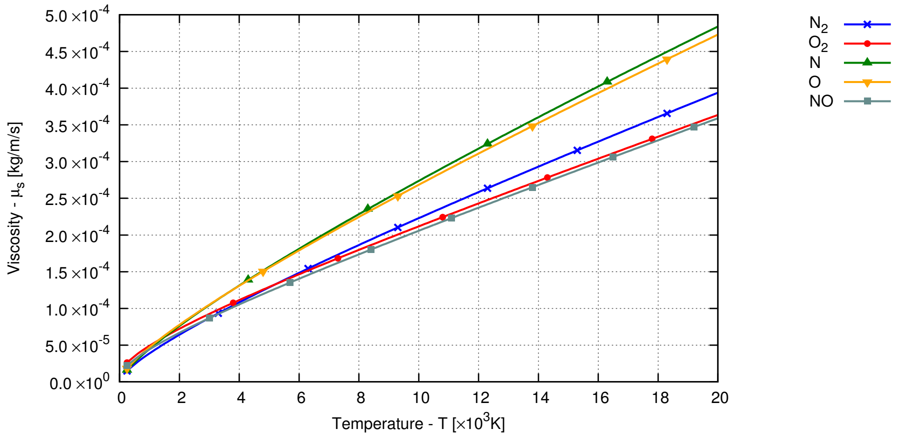

Figure B.3: *Viscosity coefficients* μ_s *of neutral species*

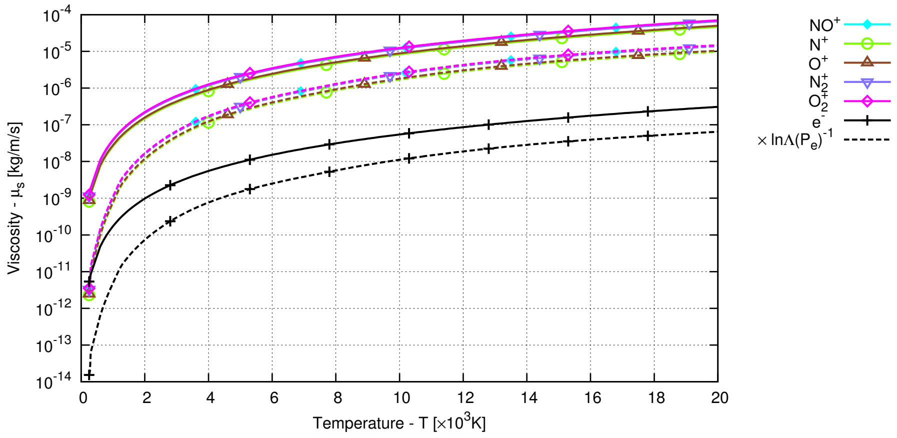

Figure B.4: *Viscosity coefficients* μ_s *of charged species, with shielding effect correction* $(\ln \Lambda(P_{\mathrm{e}})^{-1})$ *for equilibrium air 1 atm*

B.3 Thermal Conductivities

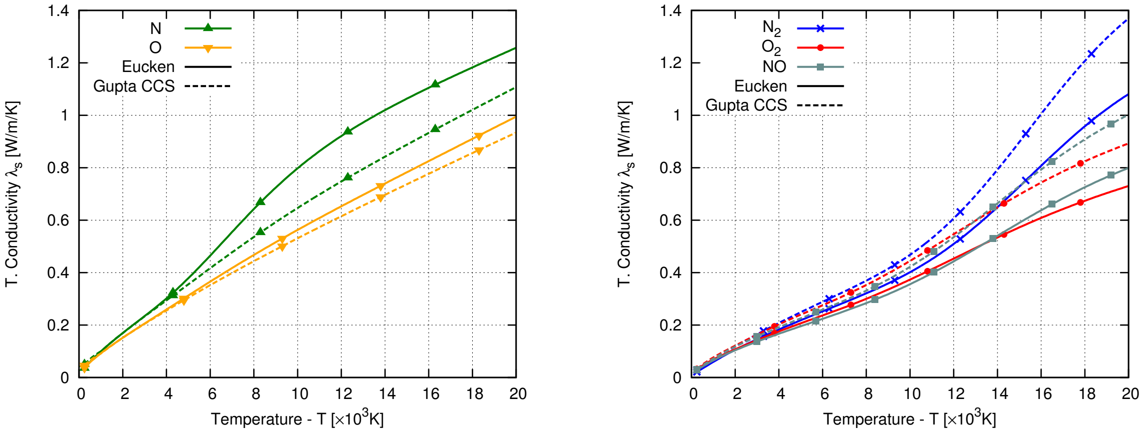

(a) Atomic Species (b) Molecular Species

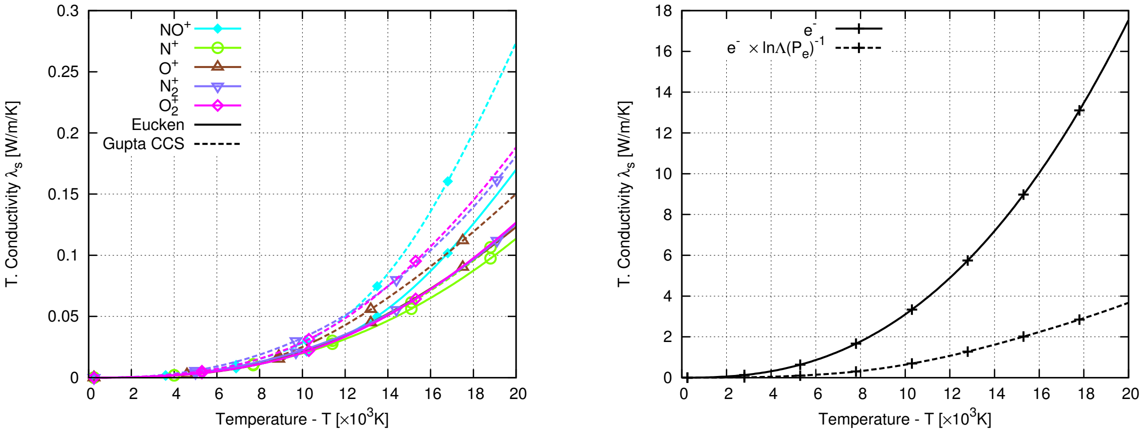

(c) Ionic Species (d) Electrons

Figure B.5: *Total thermal conductivities per species. Comparison between the Eucken relation (eq.* (2.11)*) and Collision Cross-Sections model (eq. 2.31)*